SANDIA REPORT
SAND200X-XXXX
Unlimited Release
Printed December 2018

Transient Thermal Analysis of Calorimeters Used in Characterization of the ACRR Radiation Environments

Elliott A. Pelfrey, Edward J. Parma, William J. Martin, and Curtis D. Peters

Prepared by
Sandia National Laboratories
Albuquerque, New Mexico 87185 and Livermore, California 94550

Sandia National Laboratories is a multimission laboratory managed and operated by National Technology and Engineering Solutions of Sandia LLC, a wholly owned subsidiary of Honeywell International Inc. for the U.S. Department of Energy's National Nuclear Security Administration under contract DE-NA0003525.

Issued by Sandia National Laboratories, operated for the United States Department of Energy by Sandia Corporation.

Available to DOE and DOE contractors from
U.S. Department of Energy
Office of Scientific and Technical Information
P.O. Box 62
Oak Ridge, TN 37831

Telephone: (865) 576-8401
Facsimile: (865) 576-5728
E-Mail: reports@osti.gov
Online ordering: http://www.osti.gov/scitech

Available to the public from
U.S. Department of Commerce
National Technical Information Service
5301 Shawnee Rd
Alexandria, VA 22312

Telephone: (800) 553-6847
Facsimile: (703) 605-6900
E-Mail: orders@ntis.gov
Online order: http://www.ntis.gov/search

SAND200X-XXXX
Unlimited Release
Printed December 2018

Transient Thermal Analysis of Calorimeters Used in Characterization of the ACRR Radiation Environments

Elliott A. Pelfrey, Edward J. Parma, William J. Martin, and Curtis D. Peters

Applied Nuclear Technologies Department
Sandia National Laboratories
P.O. Box 5800
Albuquerque, New Mexico 87185-1146

Abstract

Silicon calorimeters have been used for active radiation dosimetry in the central cavity of the Annular Core Research Reactor (ACRR) for over a decade. Recently, there has been interest in using other materials for calorimetry to accurately measure the prompt gamma-ray energy deposition in the mixed neutron and gamma-ray environment. The calorimeters used in the ACRR use a thermocouple (TC) to measure the change in temperature of specific materials in the radiation environment. The temperature change is related to the instantaneous dose received by the material in a pulse-transient operation. SOLIDWORKS Simulation and ANSYS Mechanical were used to model the calorimeter and analyze the thermal behavior under pulse-transient conditions. This report compares the results from modeling to experimental results for selected calorimeter materials and radiation environments. These materials include bismuth, tin, zirconium, and silicon. Calorimeters assembled with each material were irradiated in the ACRR central cavity in the free-field, LB44, CdPoly, and PLG radiation environments. The neutronics code Monte-Carlo N-Particle (MCNP) was used to calculate the neutron and gamma-ray response of the calorimeter materials at the experimental locations in the central cavity. Different response tallies were used and found to give different results for the gamma-ray energy deposition. It was determined that performing the neutron/gamma-ray/electron transport in MCNP using the *F8 electron tally gave the overall best agreement with the experimental results. The *F8 tally, however, is much more computationally intensive than the neutron/gamma-ray transport calculations. Also, this report contains parametric analyses that examine the ways to improve the current design of the calorimeters. One finding from the parametric analysis was that the TC should be placed closer to the outer radius of the disks to obtain a measurement closer to the maximum temperature of the disk. Also, the parametric analysis showed that the most dominant mechanism of heat loss in the calorimeters is conduction through the alumina posts. In future designs, the conduction should be minimized to reduce the effect of heat loss on the measurements.

Acknowledgments

The authors would like to thank Rodney Keith for obtaining the temperature-dependent specific heat data for the analysis. The authors would also like to acknowledge Tommy Ball for his support during the project.

Contents

Acknowledgments 4
Contents 5
Figures 6
Tables 7
Acronyms and Abbreviations 8
1 Introduction 9
1.1 Annular Core Research Reactor 9
1.2 Calorimeter 11
2 Simulation Setup 13
2.1 Method 13
2.2 Model Geometry 13
2.3 Power Profile 14
2.3.1 Reactor Yield Calculations 14
2.3.2 Tally Choice and Dose Calculation 14
2.3.2 *F8 Doses 20
2.3.3 Accounting for Delayed Gamma Radiation 20
2.3.4 Power Profile Shapes 21
2.3.5 Scaling 22
2.4 Material Properties 22
3 Results 24
3.1 Thermocouple Placement 24
3.1.1 Assumptions 24
3.1.2 Results 24
3.2 Thermal Sensitivity 26
3.2.1 Assumptions 26
3.2.2 Results 27
3.3 Experimental Measurements vs Simulation Results 28
3.3.1 Assumptions 28
3.3.2 Results 29
3.5 Sources of Error 34
4 Conclusion 35
Appendix A: F4, F6, *F8 Doses 36
Appendix B: Material Properties 40
Appendix C: Calorimeter Response Comparison 45
Appendix D: Specific Heat Comparison 52
Appendix E: Radiation Contributions 54
References 58

Figures

Figure 1. The ACRR with FREC-II decoupled, operating at steady-state power..... 10
Figure 2. The top loading area of the 9-inch dry central cavity..... 10
Figure 3. Assembled calorimeter. 11
Figure 4. CAD model..... 12
Figure 5. Cross-sectional views of the simulation models. 13
Figure 6. Adiabatic heating using doses from the F4, F6, and *F8 tallies compared to the experimental results for the Bi calorimeter..... 16
Figure 7. Adiabatic heating using doses from the F4, F6, and *F8 tallies compared to the experimental results for the Sn calorimeter. 17
Figure 8. Adiabatic heating using doses from the F4, F6, and *F8 tallies compared to the experimental results for the Zr calorimeter..... 18
Figure 9. Adiabatic heating using doses from the F4, F6, and *F8 tallies compared to the experimental results for the Si calorimeter. 19
Figure 10. Percent of energy released over time through delayed gamma radiation for ^{235}U for thermal fissions [11]. 21
Figure 11. Filtered vs unfiltered signal 22
Figure 12. Change in temperature vs distance from the center of the Bi, Sn, Zr, and Si disk..... 25
Figure 13. Disk offset set up. 26
Figure 14. Heat transfer sensitivity study for the Si calorimeter. 28
Figure 15. Temperature of the simulated, adiabatic and experimental data for a 25MJ, 50MJ, 100MJ pulses in FF, LB44, CdPoly and PLG for the Bi calorimeter. 30
Figure 16. Temperature of the simulated, adiabatic and experimental data for a 25MJ, 50MJ, 100MJ pulses in FF, LB44, CdPoly and PLG for the Sn calorimeter. 31
Figure 17. Temperature of the simulated, adiabatic and experimental data for a 25MJ, 50MJ, 100MJ pulses in FF, LB44, CdPoly and PLG for the Zr calorimeter. 32
Figure 18. Temperature of the simulated, adiabatic and experimental data for a 25MJ, 50MJ, 100MJ pulses in FF, LB44, CdPoly and PLG for the Si calorimeter. 33

Appendix A

Figure A.1. Results of the Bi dose for the F4, F6 and *F8 in FF, LB44, CdPoly, and PLG. 36
Figure A.2. Results of the Sn dose for the F4, F6 and *F8 in FF, LB44, CdPoly, and PLG..... 37
Figure A.3. Results of the Zr dose for the F4, F6 and *F8 in FF, LB44, CdPoly, and PLG. 38
Figure A.4. Results of the Si dose for the F4, F6 and *F8 in FF, LB44, CdPoly, and PLG. 39

Appendix C

Figure C. 1. Bi calorimeter response comparison 24.4 MJ shot. 45
Figure C. 2. Bi calorimeter response comparison 46.9 MJ shot. 46
Figure C. 3. Bi calorimeter response comparison 100.9 MJ shot. 46
Figure C. 4. Bi calorimeter response comparison 155.4 MJ shot. 47
Figure C. 5. Sn calorimeter response comparison 24.4 MJ shot..... 47
Figure C. 6. Sn calorimeter response comparison 46.9 MJ shot..... 48
Figure C. 7. Sn calorimeter response comparison 100.9 MJ shot..... 48
Figure C. 8. Sn calorimeter response comparison 155.4 MJ shot..... 49
Figure C. 9. Zr calorimeter response comparison 24.4 MJ shot. 49

Figure C. 10. Zr calorimeter response comparison 46.9 MJ shot. 50
Figure C. 11. Zr calorimeter response comparison 100.9 MJ shot. 50
Figure C. 12. Zr calorimeter response comparison 155.4 MJ shot. 51

Appendix D

Figure D. 1. Bi specific heat comparison. 52
Figure D. 2. Sn specific heat comparison. 52
Figure D. 3. Zr specific heat comparison. 53

Appendix E

Figure E. 1. Radiation contributions for the Bi Calorimeter in FF, PLG, LB44 environments.... 54
Figure E. 2. Radiation contributions for the Sn Calorimeter in FF, PLG, LB44 environments. .. 55
Figure E. 3. Radiation contributions for the Zr Calorimeter in FF, PLG, LB44 environments.... 55
Figure E. 4. Radiation contributions for the Si Calorimeter in FF, PLG, LB44 environments. ... 56
Figure E. 5. 25 MJ shot with a rod hold up time of 0.40 seconds. 56
Figure E. 6. 25 MJ shot with a rod hold up time of 0.25 seconds. 57

Tables

Table 1. Power conversion factors for Ni activation. 14
Table 2. F8* dose tally for each disk. 20
Table 3. Percent difference between max temperature and measured due to TC placement. 25
Table 4. Percent difference between max temperature and temperature measured at the TCs when the disk is offset 26
Table 5. Pulse energies 29

Acronyms and Abbreviations

Al	Aluminum
ACRR	Annular Core Research Reactor
Bi	Bismuth
CdPoly	Cadmium polyethylene
C_p	Specific heat capacity
ΔT	Change in temperature
emf	Electromotive force
ϵ	Thermal emissivity
FREC-II	Fuel Ring External Cavity-II
FF	Free field
LB44	Lead-boron 44-inch bucket
MCNP	Monte Carlo N-Particle
MJ	Megajoule
PLG	Polyethylene lead graphite
Q	Heat
rad	Unit of dose equal to 100 ergs/gram
Si	Silicon
Sn	Tin
SNL	Sandia National Laboratories
SPR-III	Sandia Pulsed Reactor III
TAV	Technical Area V
TC	Thermocouple
Zr	Zirconium

1 Introduction

Silicon calorimeters have been used for active radiation dosimetry in the central cavity of the Annular Core Research Reactor (ACRR) for over a decade. Recently, there has been interest in using other materials for calorimetry to accurately measure the gamma-ray energy deposition in the mixed neutron and gamma-ray environment. Calorimeters used in the ACRR use a thermocouple (TC) to measure the change in temperature of specific materials in the radiation environment. The change in temperature is related to the instantaneous radiation dose received by the material in a pulse-transient operation. SOLIDWORKS Simulation and ANSYS Mechanical were used to model the calorimeter and analyze the thermal behavior under pulse-transient conditions. This report presents the comparison of the modeling results to experimental results for selected calorimeter materials and radiation environments. These materials include bismuth (Bi), tin (Sn), zirconium (Zr), and silicon (Si). The calorimeters were each irradiated in the ACRR central cavity with the free-field, LB44, CdPoly, and PLG radiation environments. The neutronics code Monte-Carlo N-Particle (MCNP) was used to calculate the neutron and gamma-ray response for each calorimeter material at the experimental locations in the central cavity. Previous work by Hehr, *et al.* [1] showed that, although materials with high atomic numbers, like tantalum and tungsten, would be desirable as a gamma-ray calorimeters, they also have large radiative-capture neutron cross sections that add more complexity to the problem. Materials with lower atomic numbers have neutron scattering effects that add a large neutron-energy deposition to the calorimeter making it more difficult to distinguish the prompt gamma-ray contribution. Bi, Sn, and Zr have been found to provide adequate gamma-ray energy deposition with minimal radiative capture and neutron scattering, allowing for a temperature response that is dominated by gamma-ray contributions [1]. In this report, the nuclear reactor and the calorimeter are first introduced. Then the methods used to set up the simulation and determine the boundary conditions is documented. Finally, the results of the simulations, their comparison to the experiments, and the conclusions are presented.

1.1 Annular Core Research Reactor

The ACRR is a pool-type research reactor located within Technical Area V (TAV) at Sandia National Laboratories (SNL) in Albuquerque, New Mexico. The ACRR can operate in a pulse or steady-state mode. Most customers use the pulse-mode operation. The ACRR has been used for many different missions and experimental campaigns over the years. Historically, the reactor has been mostly used to perform electronic component testing under mixed neutron/gamma-ray pulsed environments. Other missions have included nuclear fuels testing, the development of a nuclear pumped laser, space nuclear thermal propulsion testing, and medical isotope production. One of ACRR's unique features is its 9-inch diameter dry central cavity. The ACRR can also be coupled with the Fuel Ring External Cavity-II (FREC-II) which has a 20-inch diameter dry cavity. Experiments are placed within these dry cavities and irradiated at the core centerline. Typically, the ACRR is used to perform experiments that require a high neutron fluence in pulse-mode operation. The radiation environment can be modified using spectrum modifying buckets. These buckets are composed of materials which alter the radiation environment within the central cavity. There are several buckets that are commonly used in the central cavity to adjust the free field (FF) radiation spectrum. These buckets include the 44-inch lead-boron bucket

(LB44), the polyethylene-lead-graphite (PLG) bucket, the lead-polyethylene bucket (LP) and the cadmium-polyethylene bucket (CdPoly). Characterizations of these radiation environments and more information about the ACRR and FREC-II can be found in references [2]–[6]. Figure 1 shows a picture of the ACRR during a pulse operation. In this configuration, the FREC-II is shown in the "decoupled mode," tilted back from the ACRR. Figure 2 shows the top loading area for the central cavity.

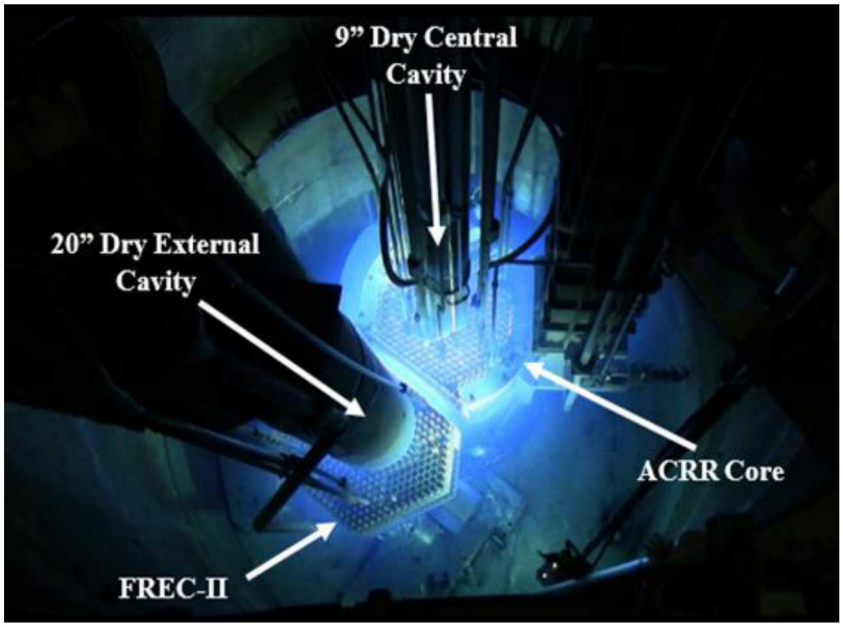

Figure 1. The ACRR with FREC-II decoupled, operating at steady-state power.

Figure 2. The top loading area of the 9-inch dry central cavity.

1.2 Calorimeter

Silicon calorimeters were originally developed to measure the instantaneous radiation dose in the ACRR central-cavity and at the Sandia Pulsed Reactor III (SPR-III). As described by Luker, *et al.* [7], the design of the calorimeter used a TC to monitor the temperature of a Si disk as it was instantly during irradiation. Although the current metal (Bi, Sn, and Zr) calorimeters use the same principles to measure the radiation, the materials of the disks were selected due to their large gamma-ray cross-sections. This allows their temperature response to be dominated by the gamma-ray energy deposition.

The current calorimeter, shown in Fig. 3, is designed to be reusable. The body of the calorimeter is made of 6061 aluminum (Al) which encases the disk, TC wires, a 0.001-inch Type-E TC, and alumina posts. The alumina posts are used to hold the disk in place by applying pressure from the top and bottom. The posts are ground to a point to minimize the thermal conduction between the posts and disk. For the calorimeters with metal disks, the TC is attached by tack welding the junction at a location 0.08 in. (2 mm) from the outer perimeter of the disk. For the Si calorimeter, the TC is held in place by sandwiching it between two Si disks. There is no assigned placement of the thermocouple junction in the Si calorimeter. The Bi, Sn, Zr, and Si disks are 0.375 in. (9.5 mm) in diameter and 0.039 in. (1 mm) thick. Models of the calorimeter are shown in Fig 4. The TC junction temperature is determined by measuring the electromotive force (emf) output voltage. Type-E extension wire extends from the TC wire to a digital oscilloscope located in the ACRR high bay. Type-E TCs are used due to their larger response(V) when compared to a Type-K TC. Other TCs could be used with similar results, however their signals may need to be amplified.

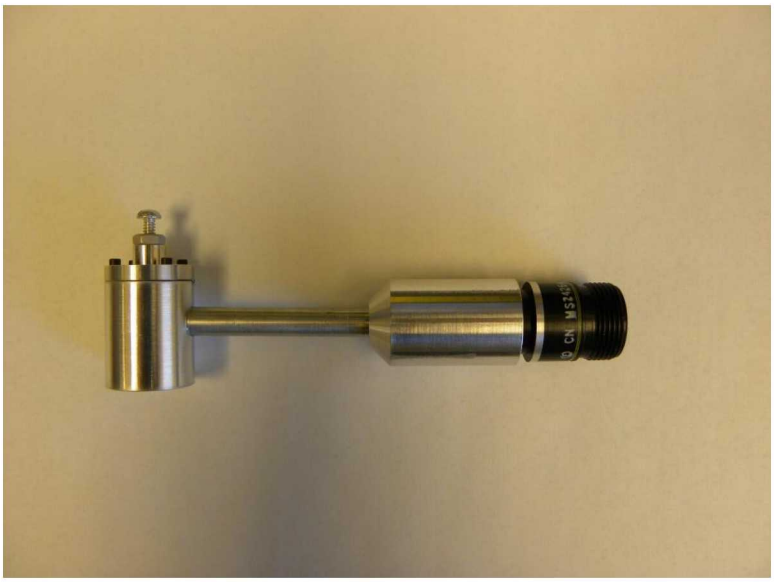

Figure 3. Assembled calorimeter.

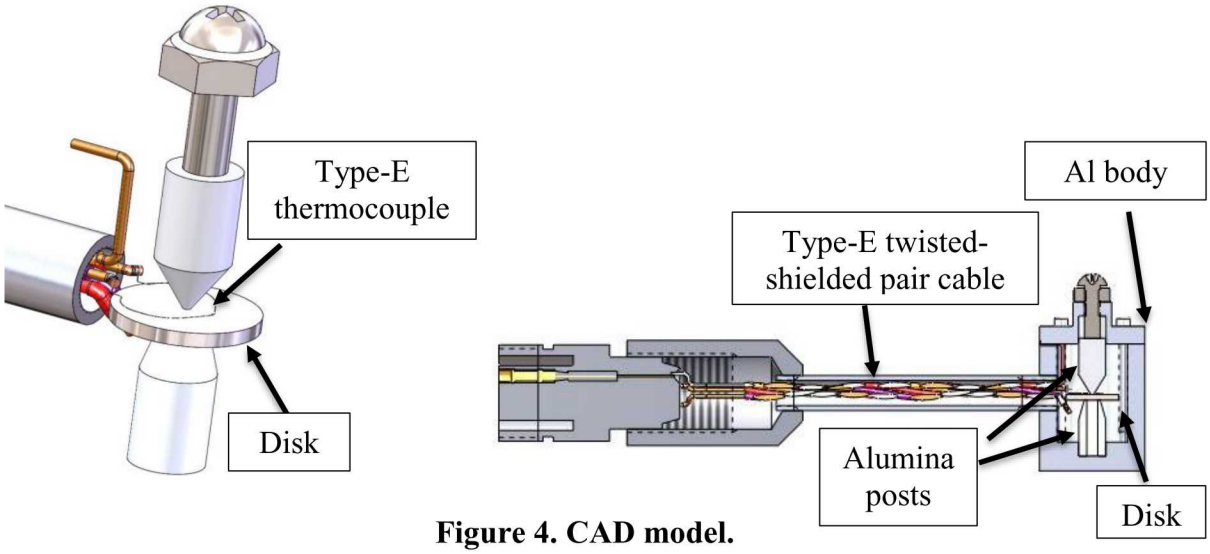

Figure 4. CAD model.

These calorimeters are not perfect calorimeters meaning they are subject to heat loss. Heat loss from the disk occurs through conduction, radiation, and convection. The degree and speed at which this occurs depends on several factors including the mass, thermal conductivity, specific heats of the calorimeter disk. It is also dependent on the convection within the calorimeter, contact resistance between the disks and the posts, and finally the thermal emissivity of the materials. One of the major aspects of this work is to parametrically analyze a number of these factors, including the heat transfer mechanisms (conduction, radiation, and convection) and location of the TC junction, and compare the results to adiabatic calculations. The parametric analyses give insight into how to improve the calorimeters.

2 Simulation Setup

2.1 Method

SOLIDWORKS Simulation and ANSYS Mechanical [8], [9], which are both finite element software packages, were used to perform the heat transfer simulations needed in the analyses. The finite element method is used to discretize and solve differential equations numerically that would otherwise be impossible to solve. Neither SOLIDWORKS Simulation nor ANSYS Mechanical are radiation transport codes so the energy deposited into the calorimeter by radiation was inputted as time-dependent internal power generation. The internal power generation boundary conditions for the analyses were determined using a combination of experimental and calculated information using MCNP. The experimental data came from both active and passive dosimetry which was used to calculate the dose (rad[material]/MJ) each material received. Several parametric analyses were performed to determine ways to improve the calorimeters. Also, results of the simulations were compared to experimental results to qualitatively determine how well they compare with actual calorimeter data.

2.2 Model Geometry

The full calorimeter geometry was not used in this analysis. Instead, components that were deemed to have negligible contributions to heat transfer of the disk were neglected. These consisted of components that were far from and not in contact with the disk. A parametric study demonstrated that these simplifications had no effects on the heat transfer of the disk. Figure 4 shows CAD drawings of the calorimeter. Figure 5 shows the computational model for the metal disk calorimeter and the Si disk calorimeter. The Si calorimeter differs from the metal ones in that the TC is sandwiched between two Si discs.

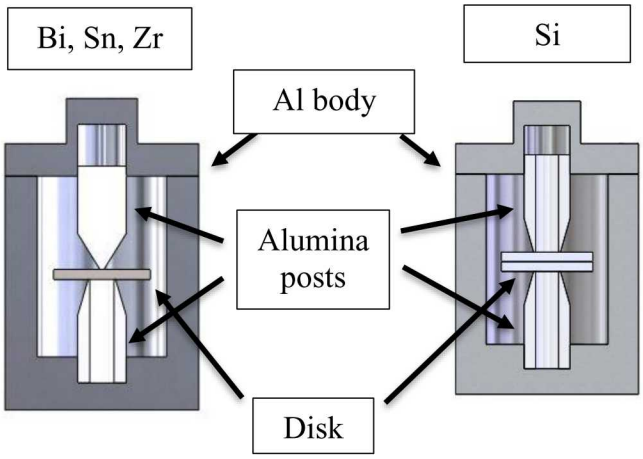

Figure 5. Cross-sectional views of the simulation models.

2.3 Power Profile

2.3.1 Reactor Yield Calculations

Nickel (Ni) foils and sulfur (S) tablets are used as passive neutron-activation dosimetry in the ACRR central cavity. These materials are considered reference fast-neutron activation standards for determining the neutron fluence in the cavity in specific locations and specific radiation environments. From the neutron fluences, the total amount of energy (MJ) emitted during the pulse can be calculated. See references [2]–[6] for more information regarding the conversion factors for the FF, CdPoly, LB44, and PLG buckets from activation to total neutron fluence and total reactor energy. Table 1 shows the conversion factors from these references that are used to convert the Ni neutron activation results to total pulse energy in MJ.

Table 1. Power conversion factors for Ni activation.

Cavity Radiation Environment	Power Conversion (MJ/Bq/$g_{Ni\text{-}58}$])	Standard Deviation (%)
FF	1.80E-03	4.1
CdPoly	2.33E-03	3.9
LB44	2.97E-03	3.9
PLG	2.17E-03	3.9

2.3.2 Tally Choice and Dose Calculation

MCNP was used to calculate the dose in rad[material]/MJ for each material. Combined with the reactor yield, the dose was used to find the amount energy that was deposited in each material during an operation in the ACRR. Within MCNP there are several tallies used to track dose [10]. The three tallies that were considered when calculating dose for this analysis were the F4, F6, and *F8 tallies. The F4 tally is a tally that tracks the flux or reaction response in a user defined cell. The F6 tally tracks the energy deposition in a user defined cell. Lastly, the *F8 tally also is an energy deposition tally however it can also account for electron transport. For more information on the different tallies see the MCNP6 user manual [10]. The F4, F6, and *F8 each yielded different results with the F4 tally generally calculating the highest dose and the *F8 calculating the lowest dose. A comparison of each dose using the different tallies is in Appendix A. Hehr, *et al.* [1] found the *F8 tally generated the dose that agreed best with experimental data.

Hehrs' results were reexamined by using the results for the F4, F6, and *F8 tallies to calculate the adiabatic change in temperature of the calorimeter disks. The change in temperatures were then compared to experimental results. The change in temperature for each dose was found using the equation $Q = mc_p\Delta T$. The amount of energy deposited (Q) was determined by multiplying the reactor yield by the dose (rad[material]/MJ) received by each material. The temperature changes calculated from these analyses were compared to experimental results of calorimeters exposed to the same yield in the reactor. The max temperatures over the first two seconds of experimental data were used in the comparison. These comparisons show how the F4,

F6 and *F8 tallies compare with each other and experimental results. If heat loss was to be accounted for, it is expected that the calculated change in temperatures would be less than those seen in the adiabatic cases.

Results for the Bi calorimeter are shown in Fig. 6. In the figures, the F4 tally resulted in the highest change in temperature with the F6 tally the second highest and the *F8 tally with the lowest. The *F8 tally provides the dose that results in change in temperatures closest to experimental results. The change in temperatures in the adiabatic analyses tended to be higher than the experimental data. This was expected seeing heat loss was not accounted for. Figure 7 shows the results for the Sn calorimeter. Like the Bi calorimeter the, the dose from the *F8 tally gave the closest results to the experimental results. The results for the Zr calorimeter are shown in Fig. 8. Unlike the Bi and Sn calorimeters, the F6 tally provided the closest temperature to the experimental results. There is no obvious reason why the F6 tally provided the most comparable result in Zr. The results for the Si analyses are displayed in Fig. 9. Unlike the Bi, Sn and Zr calorimeters, there is no clear trend for which dose produces the highest change in temperature. The doses calculated using each tally are much more precise than the results in the other calorimeters. They are also systematically lower than the experimental results. Overall, the *F8 tally provided the dose that resulted the change in temperature that was most comparable to experimental results. This corroborates the findings in Hehr, *et al.,* [1]. For this reason, the *F8 tally was used in the rest of the analyses.

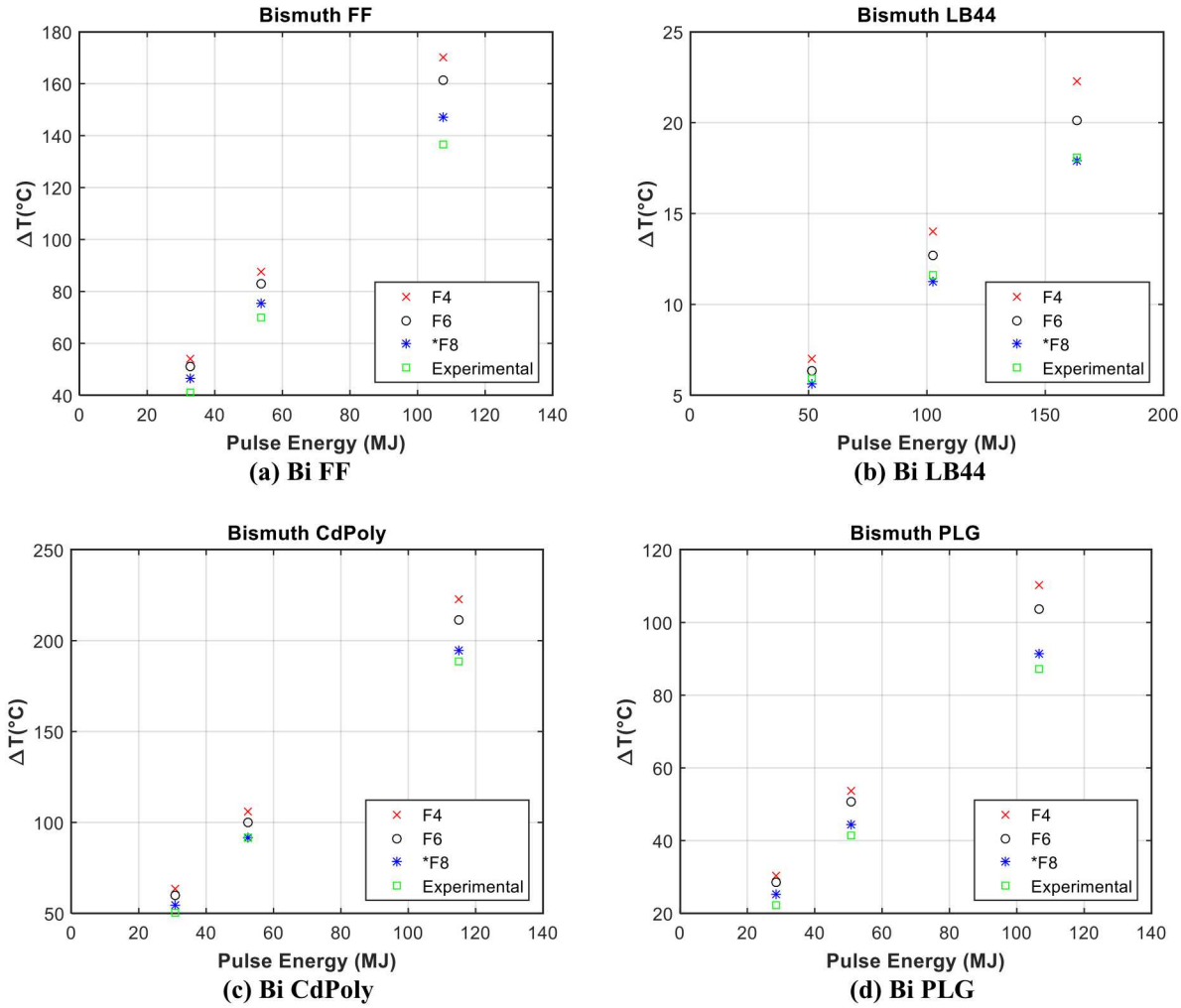

Figure 6. Adiabatic heating using doses from the F4, F6, and *F8 tallies compared to the experimental results for the Bi calorimeter.

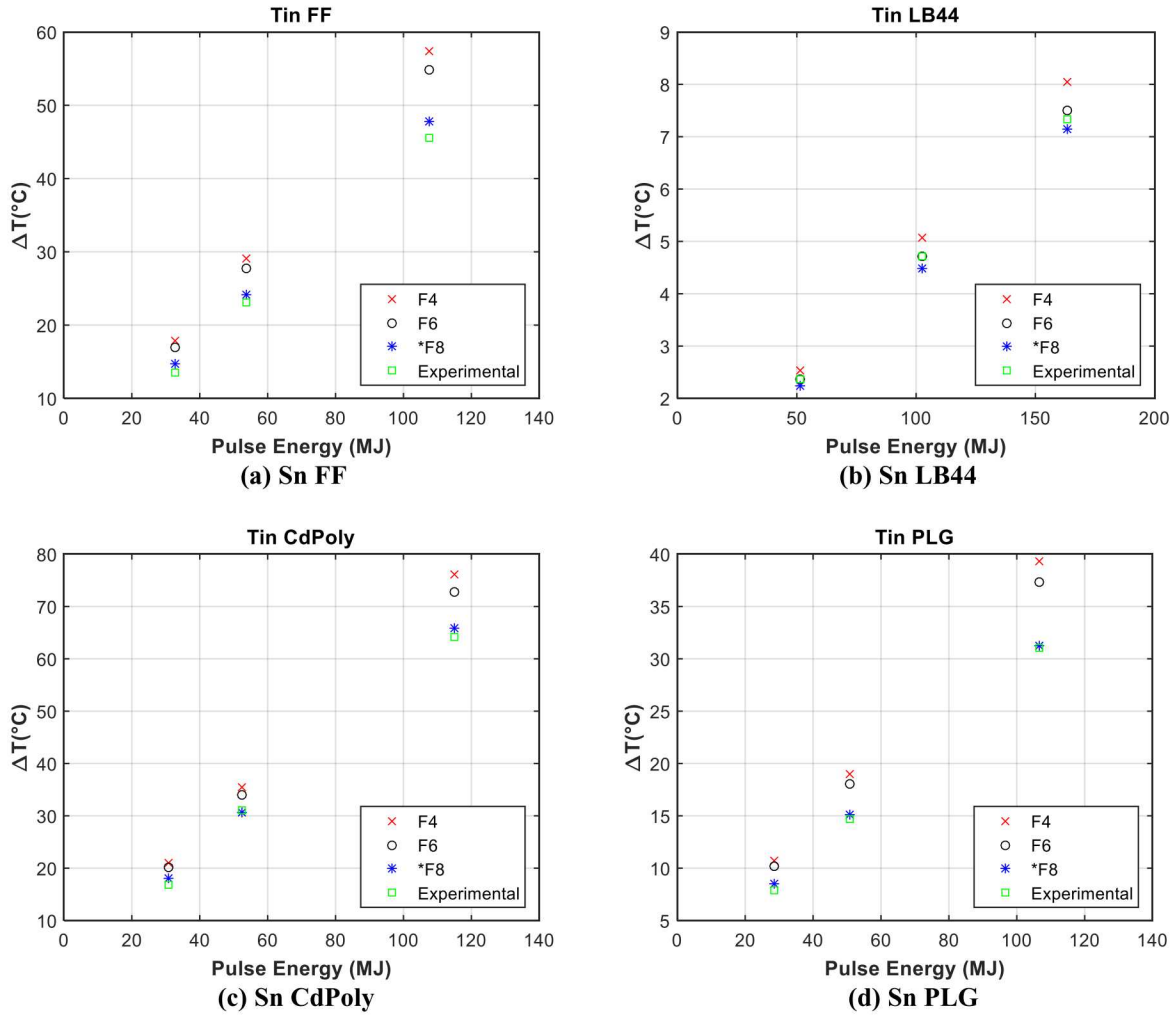

Figure 7. Adiabatic heating using doses from the F4, F6, and *F8 tallies compared to the experimental results for the Sn calorimeter.

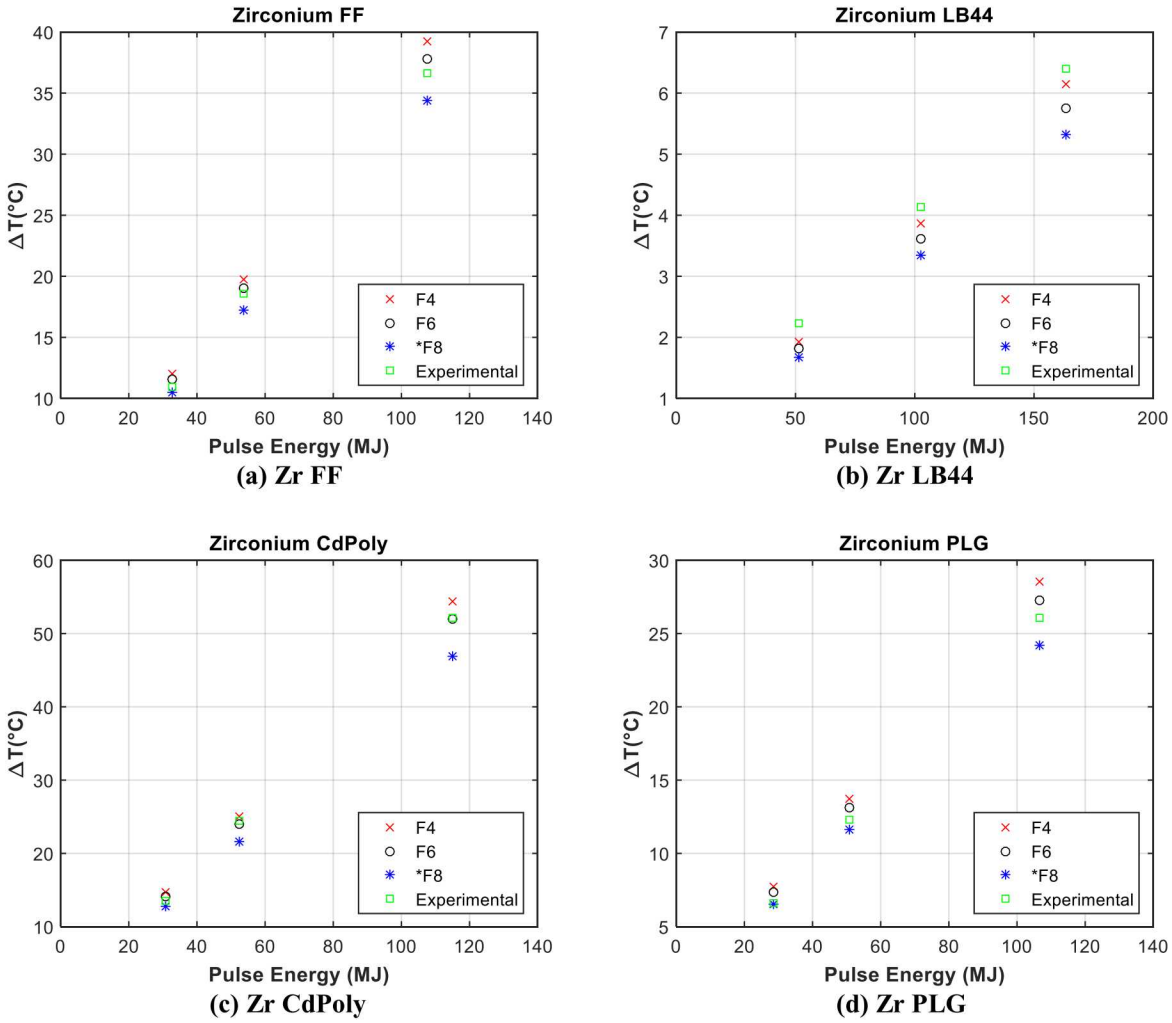

Figure 8. Adiabatic heating using doses from the F4, F6, and *F8 tallies compared to the experimental results for the Zr calorimeter.

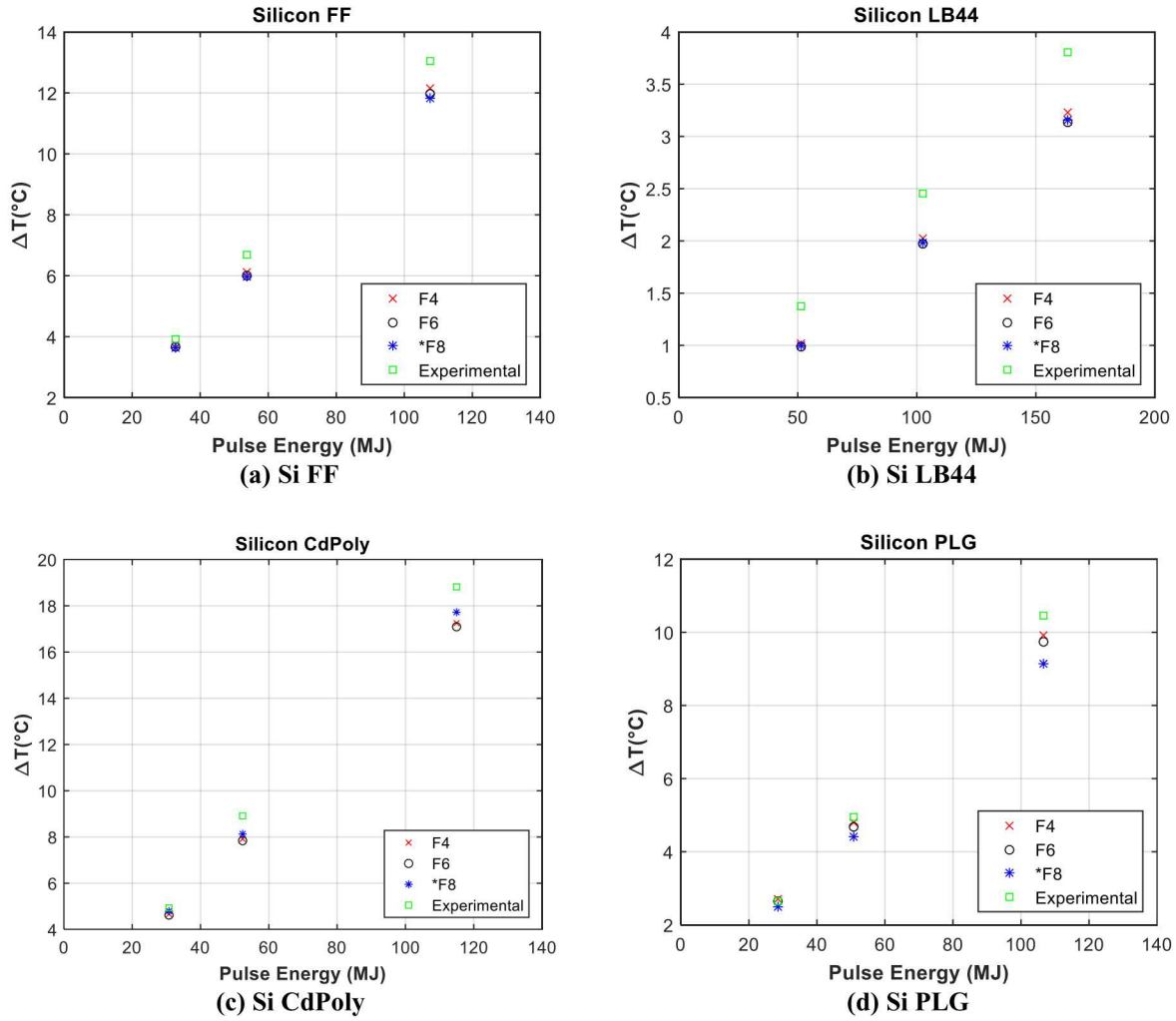

Figure 9. Adiabatic heating using doses from the F4, F6, and *F8 tallies compared to the experimental results for the Si calorimeter.

2.3.2 *F8 Doses

The doses provide the coupling between reactor yield and the energy deposition in the materials. The doses found using the *F8 tally can be found in Table 2. The uncertainty of the doses calculated in the FF, CdPoly, and PLG environments are all around 2%. The uncertainty in the dose calculations for the LB44 bucket environment is closer to 4%. The increased uncertainty for the LB44 bucket is due to the gamma-ray shielding effects of the lead. The shielding effects reduce the gamma-ray dose to the calorimeter, and requires the simulation to have a larger initial neutron population and thus increases the computational time.

Table 2. F8* dose tally for each disk.

Bucket	Total Bi Dose (rad[Bi]/MJ)	Total Zr Dose (rad[Zr]/MJ)	Total Sn Dose (rad[Sn]/MJ)	Total Si Dose (rad[Si]/MJ)	Uncertainty (%)
LB44	1.34	0.933	1.01	1.38	<4.0%
CdPoly	22.1	11.9	13.7	11.1	2.0%
FF	17.6	9.26	10.5	7.96	2.2%
PLG	10.8	6.56	6.87	6.18	2.4%

2.3.3 Accounting for Delayed Gamma Radiation

Delayed gamma radiation occurs when radioactive fission products and activation products decay emitting a gamma-ray. In the ACRR, delayed gamma radiation can be responsible for up to 31.2% of the energy deposited into a calorimeter. The contributions due to each form of radiation can be found in Appendix D. Although delayed gamma radiation can be almost a third of the total energy deposited into the calorimeter, its contribution to the temperature response of the calorimeter is negligible. This was determined using work performed by Lane and Parma on the delayed fission gamma-ray characteristics of uranium-235 (^{235}U) [11]. In their work they examined the total delayed gamma radiation energy over time. Figure 10 shows the amount of gamma-ray energy released over time by ^{235}U. From experimental data collected from the calorimeters, it was observed that the metal disks in the calorimeters begin to decline in temperature 0.85 seconds after the pulse. According to Fig. 10, approximately 5.79% of the total 31.2% contribution of delayed gamma radiation has been emitted at 0.85 seconds. This equates to 1.7% percent of the energy experienced by the calorimeter before heat loss dominates in the disk. A 1.7% contribution is considered negligible in this analysis. The rest of the delayed gamma-ray energy is deposited after heat loss dominates in the calorimeters. Because that energy does not contribute to the max temperature of the calorimeter, it is also neglected.

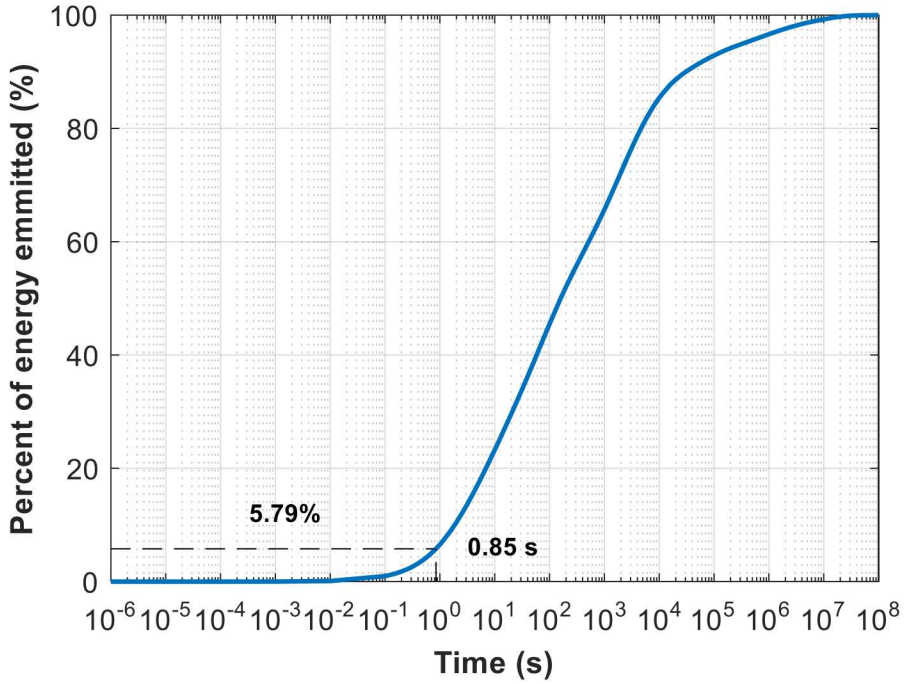

Figure 10. Percent of energy released over time through delayed gamma radiation for ^{235}U for thermal fissions [11].

2.3.4 Power Profile Shapes

The shape of the power profile inputted into SOLIDWORKS Simulation was captured using a self-powered neutron detector (SPND). SPNDs are used at the ACRR as part of the reactor diagnostics. They are used to measure the time dependent neutron flux in radiation environments. For more information on SPNDs see reference [12]. The neutron flux also corresponds to the prompt gamma-ray flux due to the fact both neutrons and gamma rays are emitted simultaneously during fission. The SPNDs had to be processed before being used to represent the radiation profile. The first step in processing the SPND before being scaled was to reduce the amount of noise in the signal. To smooth the SPND a Savitzky-Golay filter was used. Savitzky-Golay filters use a localized least square fit of a polynomial to approximate the value of the smoothed point at the center of a specified window of points. The window is then moved across the entire signal to determine the smoothed value at each point[13]. Figure 11 shows the noise in the signal both before and after filtering. Although some noise was still present in the filtered signal, the filter reduced the noise by one order of magnitude. The second and final step was removing an offset in the SPND signal. Before a pulse, the ACRR is operated at steady-state and then rod-worth operation are performed which are recorded in the signal. Even though there is radiation in the pre-pulse diagnostics, the effects on the temperatures in calorimeter are assumed to be negligible.

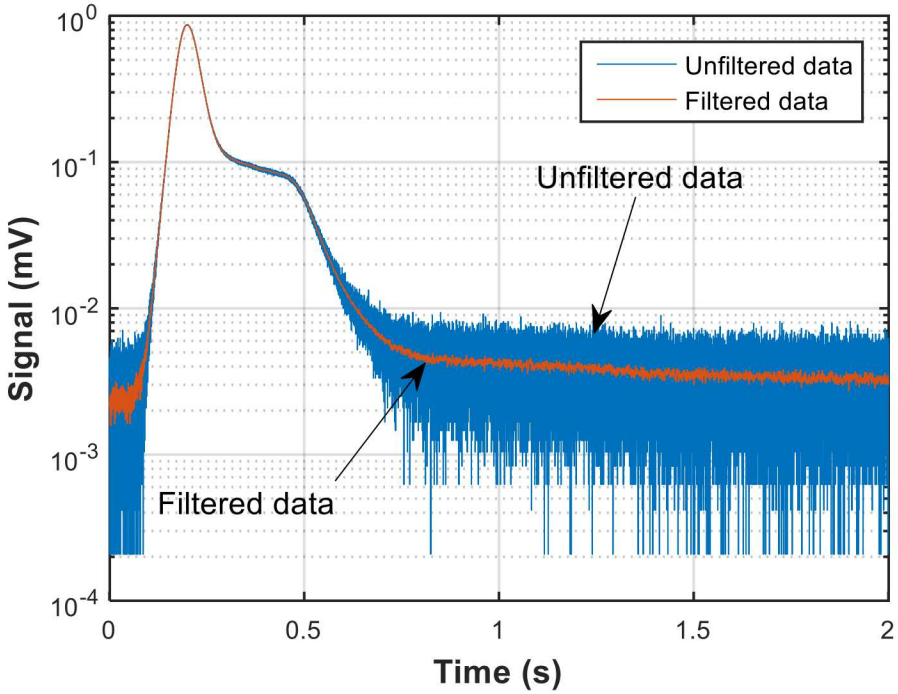

Figure 11. Filtered vs unfiltered signal

2.3.5 Scaling

The SPND was scaled to represent the time-dependent rate of energy deposition into each component of the calorimeter. The amount energy deposited in each material was found by multiplying the dose (rad[material]/MJ) and the total energy of the pulse (MJ). The time-dependent gamma radiation profile was scaled for each material such that its integral was equal to the total energy deposited in that material. By scaling the profile, the units of the signal were converted from mV/s to watts. The calculation can be seen below.

$$Power\ Profile = \frac{pulse\ energy\ from\ nickel\ foil[MJ] * MCNP\ dose[rad/MJ] * mass[kg]}{SPND\ integral} * SPND\ signal$$

The mass corresponds to the mass of each component of the calorimeter.

2.4 Material Properties

The thermophysical properties of the materials were taken from a variety of sources. The temperature-dependent specific heats of the Bi, Sn, and Zr disks were evaluated by Thermophysical Properties Research Laboratory, Inc. (TPRL) [14]. TPRL used a Perkin-Elmer Differential Scanning Calorimeter with sapphire as the reference material to measure the specific

heats. Luker *et al.,* published the temperature-dependent specific heat of the Si used in the calorimeter [7]. The material properties of the alumina were taken from the supplier, Ortech Advanced Ceramics [15]. SOLIDWORKS Simulation contains the material properties for many different materials. The built in SOLIDWORK Simulation material properties were used for Al in the simulations. A temperature-dependent thermal conductivity was also used for each of the metal disks, which was found using CINDAS LLC "Thermophysical Properties of Matter Database" [16]–[18]. Also, the thermal emissivity (ϵ) of Bi and Sn were taken from the "Table of Total Emissivity" by OMEGA [19]. The emissivity of Si and Zr were assumed to be 1. The thermal material properties used in the analyses are found in Appendix B.

3 Results

3.1 Thermocouple Placement

3.1.1 Assumptions

The following assumptions were made when performing this analysis.

- Constant material density;
- Convection of 5W/m^2K;
- Initial temperature of 23°C;
- Contact resistance of 0.0001 ((K*m^2)/W) between the posts and the disk;
- Delayed gamma-ray contributions were negligible;
- Perfect contact between the TC and the disk;
- Surface to ambient radiation of the disks.

3.1.2 Results

Thermocouple position sensitivity studies were performed to demonstrate how different placements of the TC junction could affect the measured temperature of the disk. The studies were performed specifically on a 100 MJ pulse in the CdPoly bucket. This case was chosen because materials in the CdPoly bucket experience a large gamma-ray flux creating large changes in temperature. With larger changes in temperature, the effects of heat transfer are more pronounced giving a good idea of the worst-case temperature distributions. Also, the lower margin for contact resistance was used to demonstrate the most extreme but possible temperature gradient. In Fig. 12 the temperature of the disk is plotted at distances increasing radially from the center of the disk. Also, the maximum temperature of the disk in the analyses is represented by a horizontal red line. Figure 12 shows that the temperature of the disk increases further from the center of the disk. This is due to conduction through the alumina posts. The disk and the alumina heat differently in the radiation. The temperature difference between the alumina and the disks causes conduction. The effect of conduction is most noticeable in the Bi disk. This is likely because the Bi disk experiences the highest change in temperature, increasing the rate of conduction.

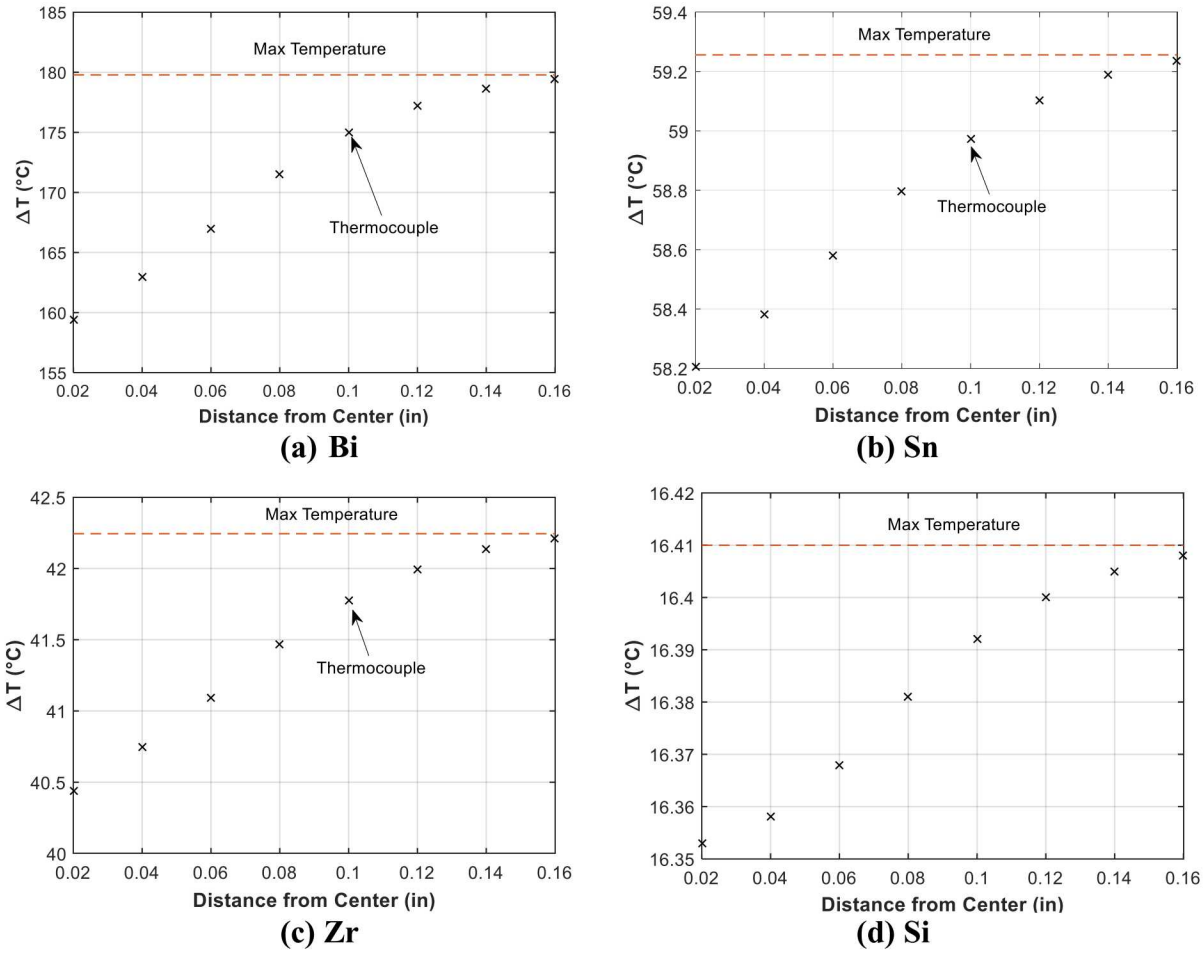

Figure 12. Change in temperature vs distance from the center of the Bi, Sn, Zr, and Si disk.

If the TC is placed 0.08 inches from the outer edge, as is currently practiced, there will be a difference between the true maximum temperature of the disk and the measured temperature. Table 3 shows these percent differences. Silicon is not included in this table because there is no fixed position for the thermocouple.

Table 3. Percent difference between max temperature and measured due to TC placement.

Calorimeter	0.08 In. from Edge (%)
Bi	2.72
Zr	1.1
Sn	0.47

During assembly of the calorimeters, there is no process that ensures that the disk is held directly in its center. The purpose of this analysis was to examine how the measured temperature would be affected if the disk was nearly touching the Al body. The analysis was performed with the outer perimeter of the disk 0.0025 in. from the Al body, at its closest point. In this analysis, the temperature of the disk was still recorded 0.08 inches from the outer edge of the disk as shown in Fig. 13.

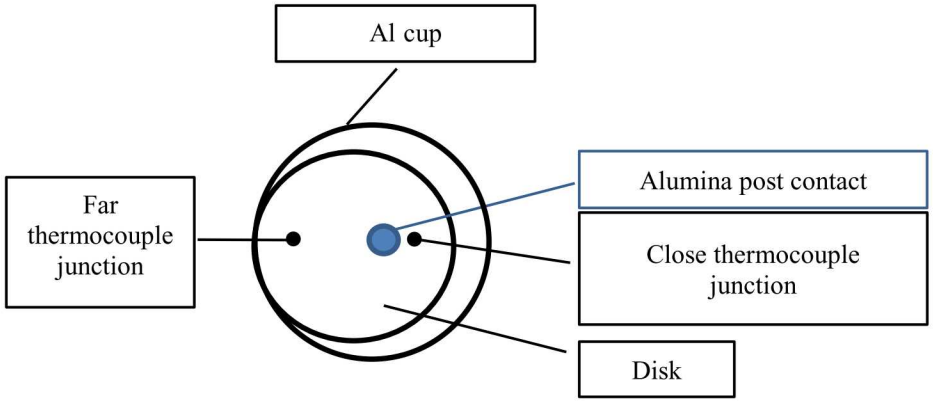

Figure 13. Disk offset set up.

Table 4 shows the results of this analysis. As Table 4 shows, the consequence of measuring a temperature closer to the disk due to an offset can be as much as 10.6% for the Bi calorimeter.

Table 4. Percent difference between max temperature and temperature measured at the TCs when the disk is offset.

Calorimeter	Close Junction (%)	Far Junction (%)
Bi	10.6	0.787
Zr	4.86	0.42
Sn	2.89	0.31

When the calorimeter is assembled, the position of the disk between the posts is not controlled. The variation of the disk placement can increase the uncertainty of the temperature measurement. Placing the thermocouple toward the outer edge of the disk can decrease the uncertainty of the measurement. In future calorimeter fabrications, this modification should be made.

3.2 Thermal Sensitivity

3.2.1 Assumptions

The following assumptions were made when performing this analysis.

- Constant material density;
- Initial temperature of 23°C;
- A contact resistance of 0 ($(K*m^2)/W$) between the posts and the disk in the conduction analysis;
- Delayed gamma-ray contributions were negligible;
- Perfect contact between the TC and the disk;
- Surface to ambient radiation of the disks;
- Thermal emissivity of 1.

3.2.2 Results

A sensitivity study was performed to qualitatively analyze the effects of each mechanism of heat transfer: conduction, radiation, and convection. The purpose of this analysis was to determine which mechanisms cause the most heat loss so that they could be minimized in future iterations of the calorimeter. It was also performed to ensure that all mechanisms of heat transfer were properly accounted for in the full thermal analysis. In this study, conduction, radiation and convection were considered individually. The analyses were performed on the each of the Bi, Si, Sn, and Zr calorimeters. The energy deposition was assumed to end instantaneously to avoid the deposition rate effecting the rate of heat loss.

The amount of energy deposited in these analyses was equivalent to the energy deposition of a 100 MJ pulse in the CdPoly bucket. The emissivity and contact resistance were set to 1 and 0 $W/(m^2K)$ respectively. Simulations with these values represent the maximum heat transfer possible by radiation and conduction. The convection coefficients were assumed to be 5 W/(m-K) which was approximated from a correlation estimating convection coefficients using the characteristic length of a cylinder and change in temperature as shown in Eqn. 1 [20]. In Eqn. 1 h is the convection coefficient, ΔT is difference in temperature between the bulk air and the cylinder, and L is the characteristic length of the cylinder.

$$h = 1.42\left(\frac{\Delta T}{L}\right)^{0.25} \qquad \text{Eqn. 1}$$

Figure 14 shows plots of the temperature response of the Bi, Sn, Zr, and Si disks with respect to time. In the plots, the more negative the slope of a line, the faster the disk is losing heat. Figure 14 shows that conduction through the posts plays the largest role on heat loss in all the calorimeters. Figure 14 (d) shows that the Si calorimeter is the least affected by all mechanisms of heat loss due to its low temperature response to radiation and the fact that the alumina posts have a similar radiation cross-section and thus similar heating as the Si disk.

The thermal sensitivity study showed that the largest contributor to heat loss was conduction through the alumina posts. To make the calorimeters more accurate, conduction is the first mechanism of heat transfer to reduce. It can be minimized by choosing less conductive materials to support it, reducing the contact area, or redesigning how the disks are supported within the calorimeter.

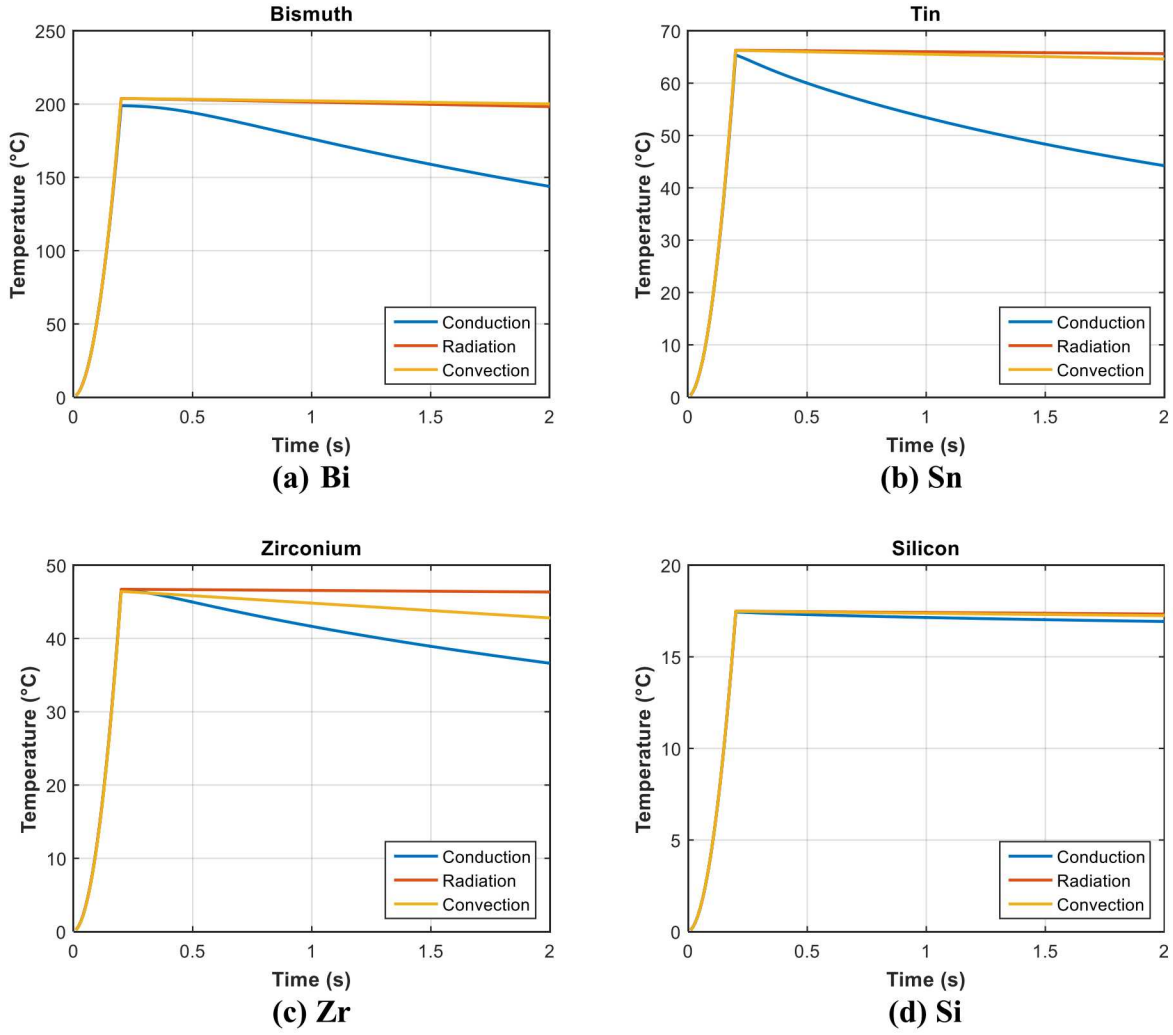

Figure 14. Heat transfer sensitivity study for the Si calorimeter.

3.3 Experimental Measurements vs Simulation Results

3.3.1 Assumptions

The following assumptions were made when performing this analysis.

- Constant material density;
- No convection;
- Initial temperature of 23°C;
- A contact resistance of 0.009 ((K*m^2)/W) between the posts and the disk;
- Delayed gamma-ray contributions were negligible;
- Perfect contact between the TC and the disk;
- Surface to ambient radiation of the disks.

3.3.2 Results

Experimental results are compared to simulation results in Figs. 22-36. The comparisons were made to validate the simulations. Each figure contains the results from three yields. The pulse energies are shown in Table 5.

Table 5. Pulse energies

Environment	Small (MJ)	Medium (MJ)	Large (MJ)
FF	32.58	53.62	107.5
LB44	51.24	102.4	163.3
CdPoly	30.76	52.32	115.0
PLG	28.58	50.91	106.6

In the FF, CdPoly, and PLG radiation environments pulses of approximately 25MJ, 50MJ, and 100MJ were performed. The LB44 environment required larger pulses to yield significant changes in temperature due to gamma radiation attenuation caused by the lead. For each pulse energy, there are three plots; the experimental results, an adiabatic simulation with no heat loss, and a simulation with heat loss. The uncertainty which is introduced when determining the pulse energy from the Ni activation foil is displayed on the adiabatic simulation.

Figure 15 shows that the Bi simulation results compared favorably to the experimental results. In each bucket, the peak experimental temperature was within the uncertainty. The rate of heat loss in the simulation was different than that for the experiment. This is likely due to a different contact resistance or an offset of the disk. Figure 16 shows the experimental vs simulation results for the Sn calorimeter. As with the Bi calorimeters, the rate of heat loss in the simulation was not consistent with the experimental results. This is also likely due to different contact resitances in the simulation and experiment or an offset in the disk in the experiment. The results of the simulations for the Zr calorimeter, seen in Fig. 17, did not show as much agreement with experimental data as was seen in the Bi and Sn calorimeters. The discrepancy is not due to any sort of heat loss in the experimental calorimeter seeing that the adiabatic simulation is lower than the experimental results. The discrepancy is also not due to positioning of the disk for the same reason. Figure 18 shows the experimental and simulation results for the Si calorimeter. The Si calorimeter, like the Zr calorimeter, did not have good agreement between the experimental and simulation results.

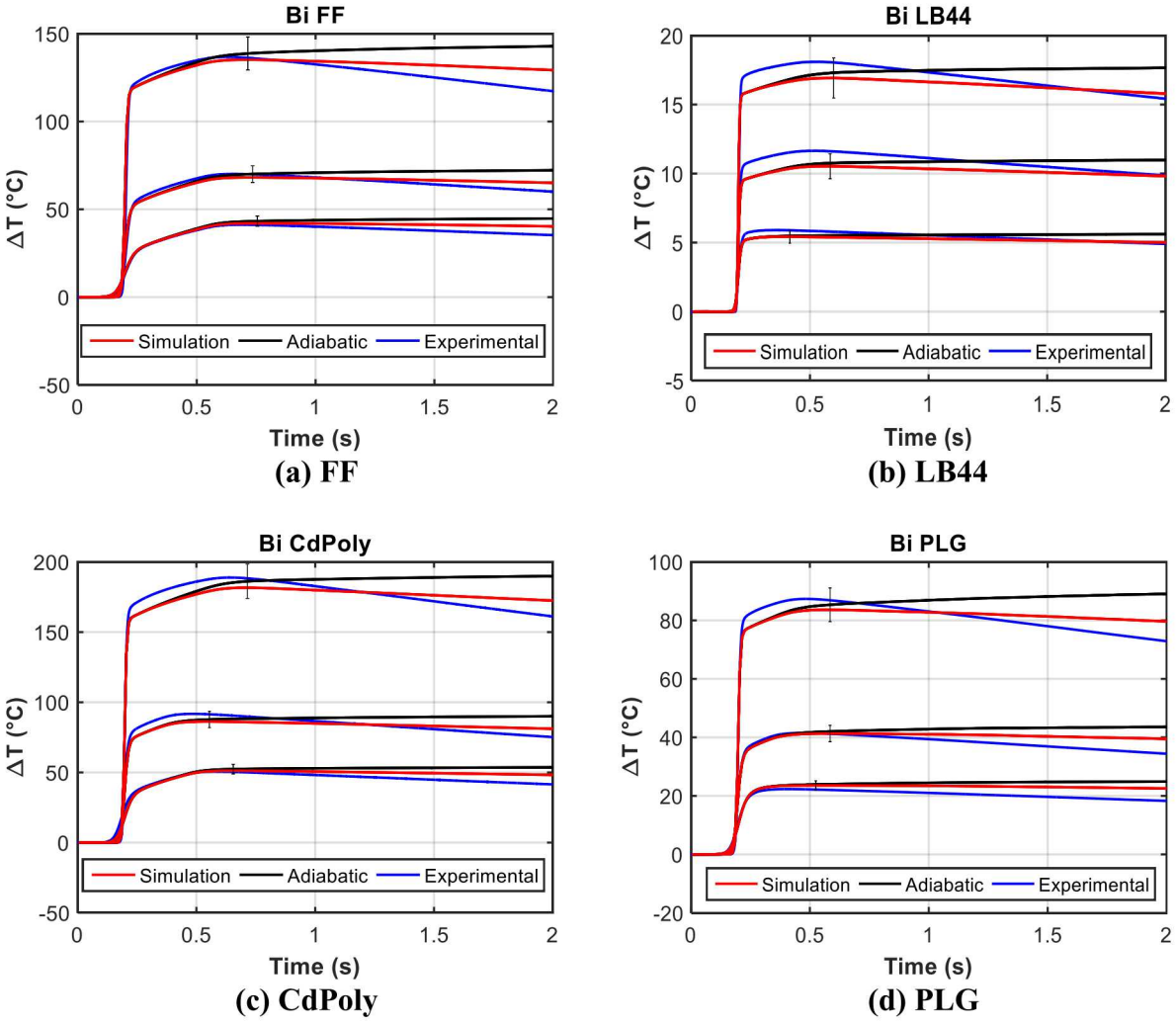

Figure 15. Temperature of the simulated, adiabatic and experimental data for a 25MJ, 50MJ, 100MJ pulses in FF, LB44, CdPoly and PLG for the Bi calorimeter.

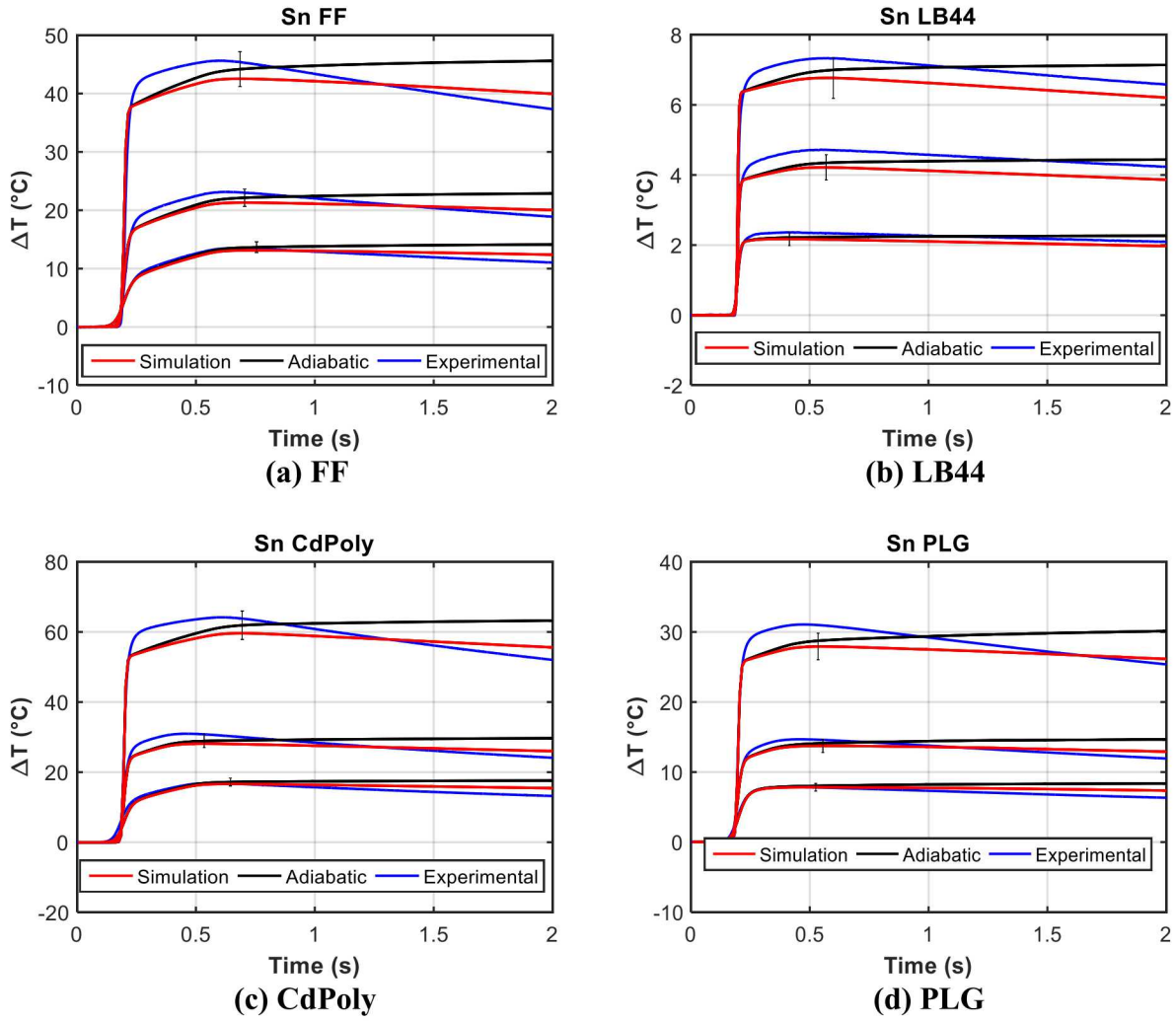

Figure 16. Temperature of the simulated, adiabatic and experimental data for a 25MJ, 50MJ, 100MJ pulses in FF, LB44, CdPoly and PLG for the Sn calorimeter.

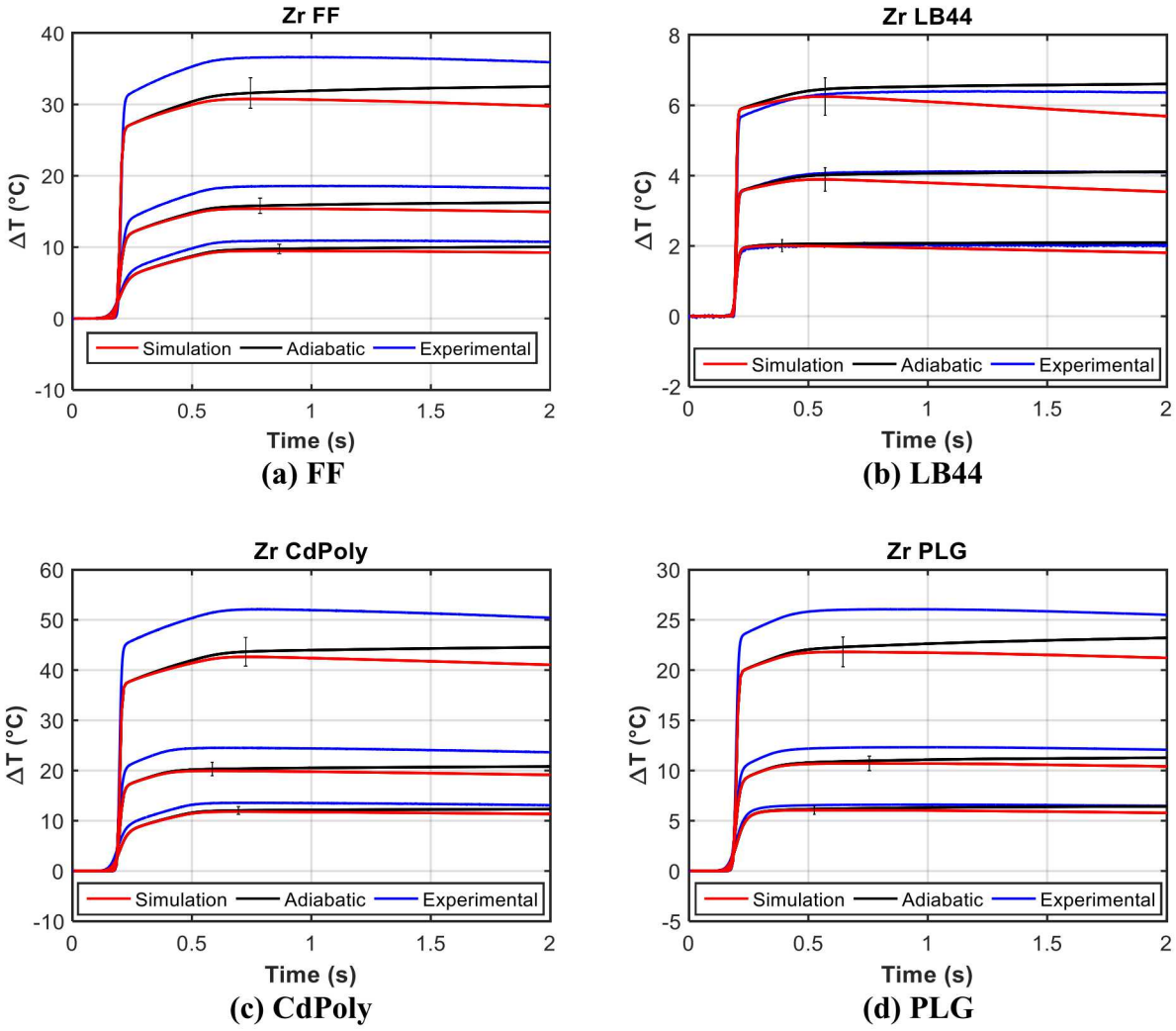

Figure 17. Temperature of the simulated, adiabatic and experimental data for a 25MJ, 50MJ, 100MJ pulses in FF, LB44, CdPoly and PLG for the Zr calorimeter.

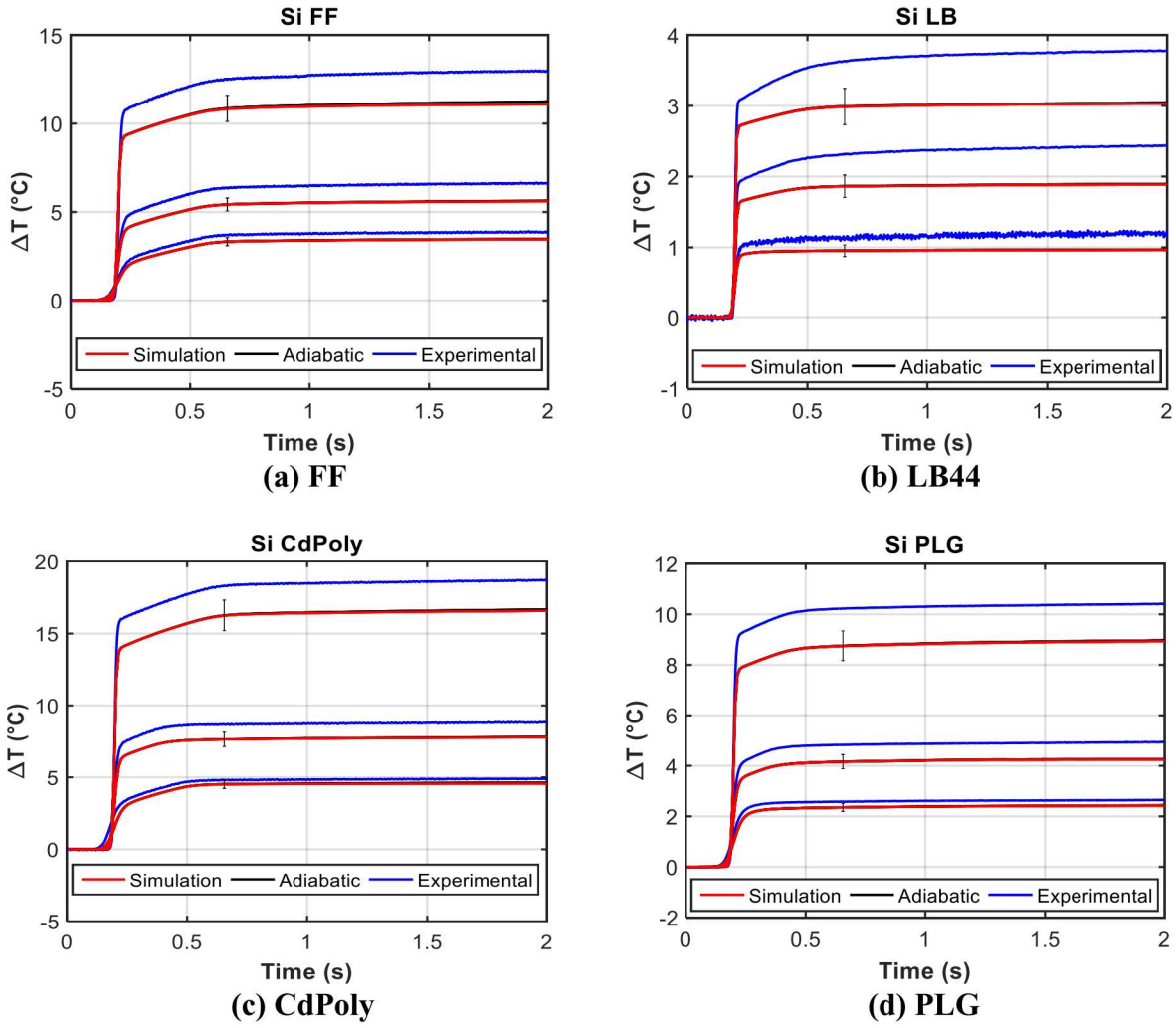

Figure 18. Temperature of the simulated, adiabatic and experimental data for a 25MJ, 50MJ, 100MJ pulses in FF, LB44, CdPoly and PLG for the Si calorimeter.

3.5 Sources of Error

Within these simulations there are several potential causes of error.

1. Parameters such as contact resistance effect the rate of heat loss and gain making the results either higher or lower than calculated in the simulation.
2. In both the measurements of the dosimetry and its conversion to MJ, there are uncertainties involved.

A combination of the causes stated above could potentially be the cause of the discrepancy between the experimental and simulation results.

4 Conclusion

Calorimeters are used in the ACRR to measure prompt radiation. Due to imperfect nature of the calorimeters, heat loss occurs which introduces uncertainty into the measurements. It is important to understand how the different mechanisms of heat transfer and variants in assembly affects the results. The results of this report demonstrate the effects of each mechanism of heat transfer, TC placement, and disk offset on the measured temperature of the calorimeter. It also compared the simulation results with experimental results.

Several conclusions can be made from the analyses. The first conclusion is that the largest contributor to heat loss in the calorimeter is conduction through the posts. Conduction should be minimized to improve the accuracy of the measurements. Secondly, the TC should be placed as close to the outer radius of the of the calorimeter as possible. The outer perimeter of the disk is less influenced by the conduction through the alumina posts. The third conclusion is that variations in the assembly such as offsets in the disk and contact resistance between the posts and disks can affect the measured temperature of the disk. This is further demonstrated in Appendix C where two calorimeters are exposed to the same pulse and have different results. Lastly, the Bi, Sn, and Zr calorimeters could each be good candidates for active gamma-ray dosimetry. Each of the three materials has a significant temperature response even in small pulses. They are, however, more effected by conduction due to the large temperature difference between the alumina posts and disks. The Si calorimeter has the largest neutron contribution making it less useful for prompt gamma-ray dosimetry. The silicon disk also has a very low temperature response making its noise to signal ratio much higher than the metal calorimeters. The Si calorimeter is, however, the least effected by heat loss due to the similar temperature response of the alumina and Si. In order to provide higher fidelity measurements, the calorimeters should be improved.

Although the *F8 tally provided the dose that most closely corresponded to experimental results, there are still questions about the proper way to calculate gamma dose using MCNP. Future work should include a comparison of MCNP dose results with results from SNL's Integrated TIGER Series (ITS), which is a coupled Monte Carlo electron and photon transport code. Also, work is underway to determine the suitability of other materials to use as supports in the calorimeter.

Appendix A: F4, F6, *F8 Doses

Three different tallying methods were considered in calculating the dose for the components of the calorimeter. Figures A.1 through A.4 compare the results from the F4, F6, and *F8 tallies. In the Bi, Zr and Sn calorimeters the F4 calculated the highest dose, F6 calculated the second highest, and *F8 calculated the lowest dose. The dose calculations for the Si calorimeter did not follow the same trend. It should be noted that change in temperature of the calorimeters are proportional to the magnitude of the dose.

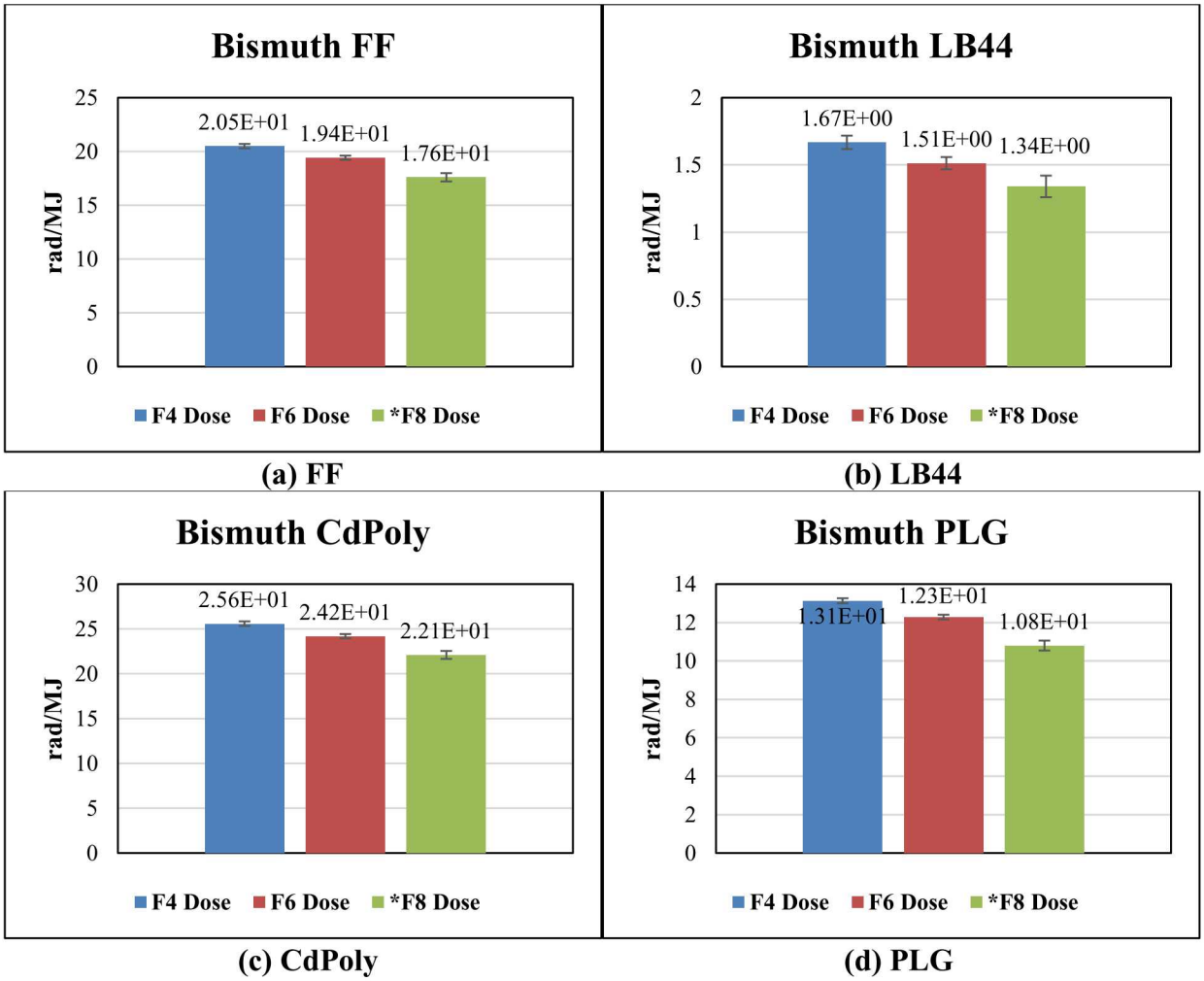

Figure A.1. Results of the Bi dose for the F4, F6 and *F8 in FF, LB44, CdPoly, and PLG.

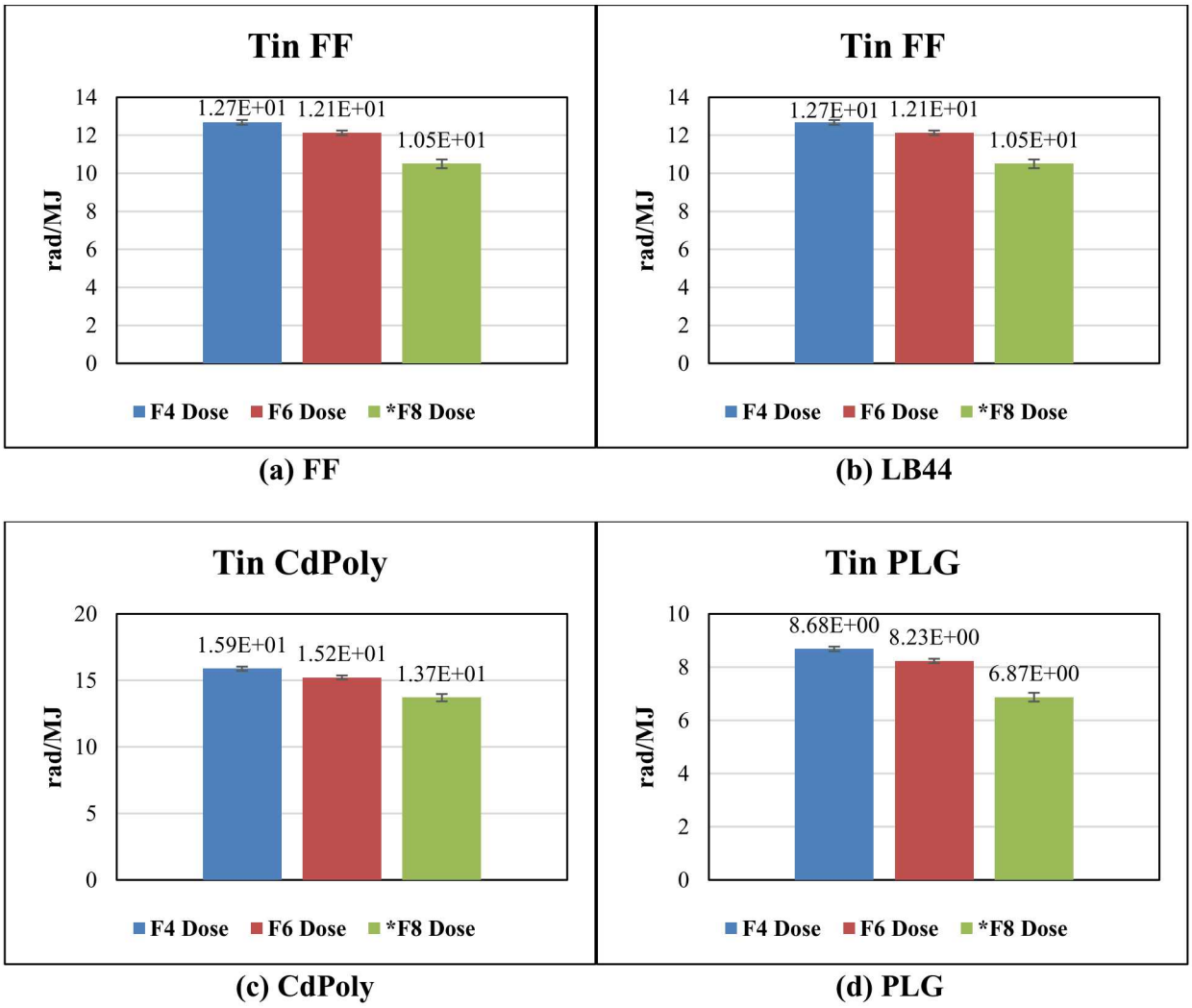

Figure A.2. Results of the Sn dose for the F4, F6 and *F8 in FF, LB44, CdPoly, and PLG.

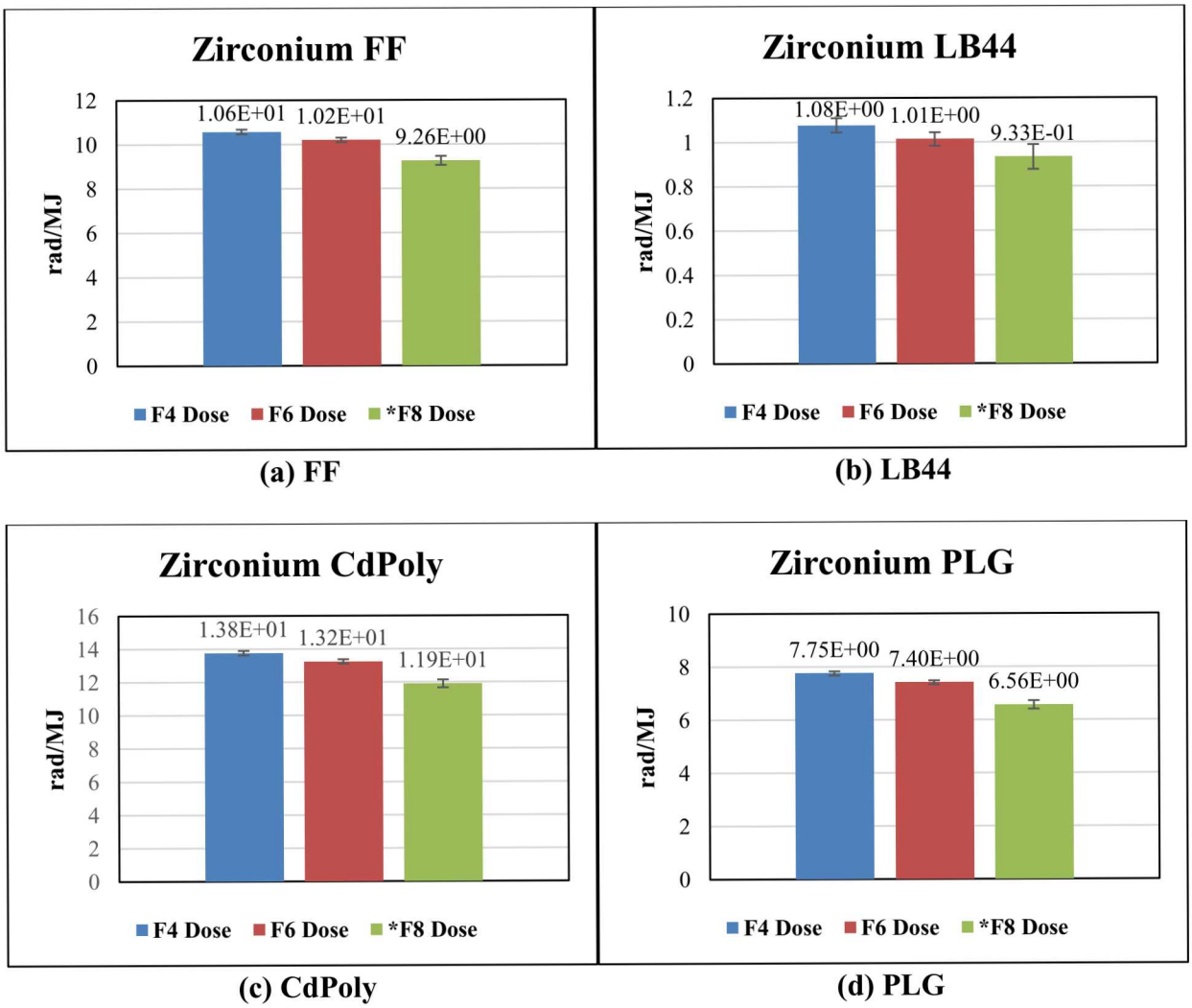

Figure A.3. Results of the Zr dose for the F4, F6 and *F8 in FF, LB44, CdPoly, and PLG.

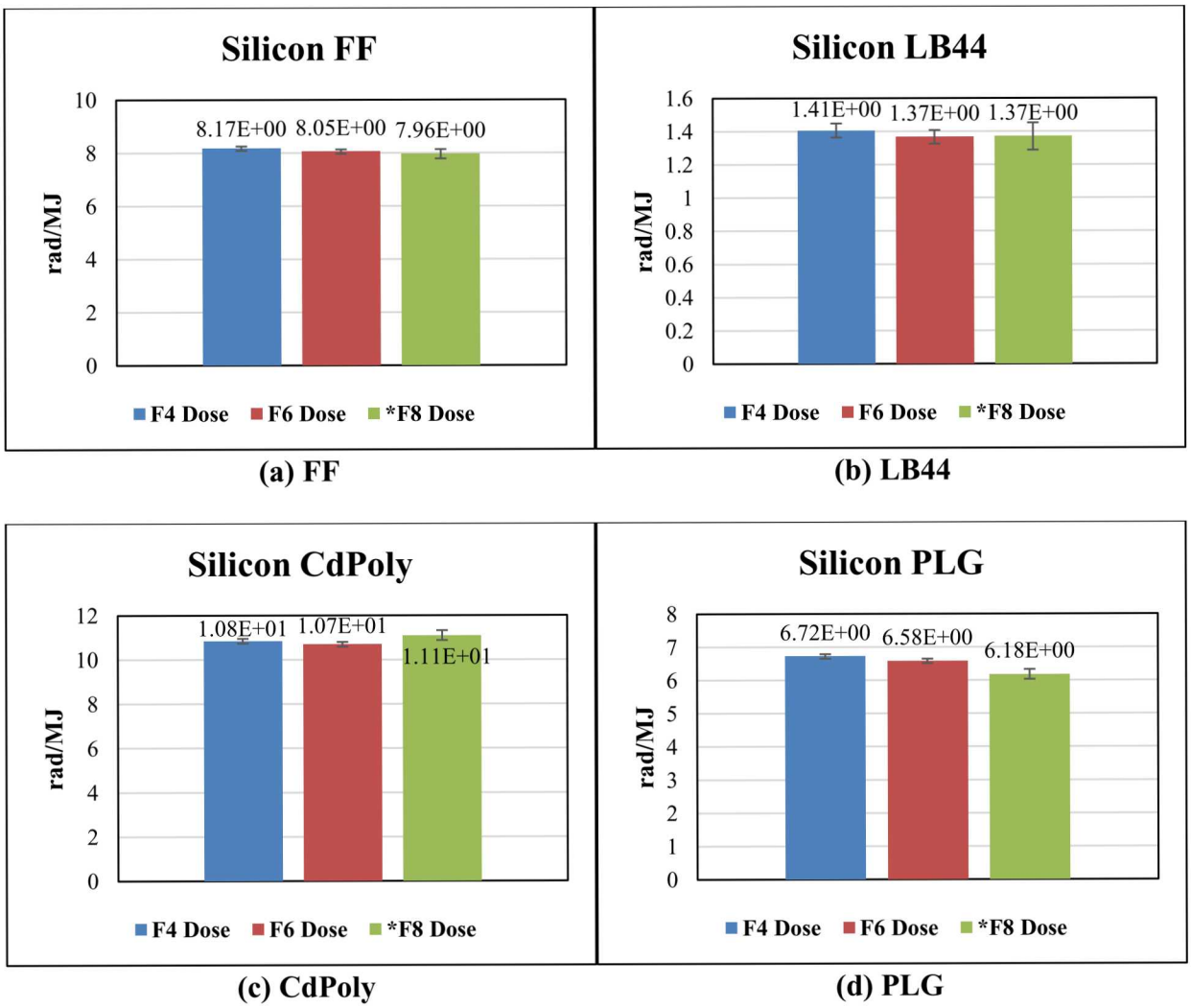

Figure A.4. Results of the Si dose for the F4, F6 and *F8 in FF, LB44, CdPoly, and PLG.

Appendix B: Material Properties

Appendix B contains the material properties used in the transient thermal analysis. The temperature dependent heat capacities for Bi, Sn and Zr all were measured by TPRL, Inc. The temperature dependent specific heat for Si was also measured by TPRL, Inc., however it was taken from Luker *et al.* [7]. The densities of each of the disks were measured. The temperature dependent thermal conductivities for the metal disks were each found in the CINDAS database[16]–[18]. All of the material properties for the Al were provided by SOLIDWORKS Simulation. The material properties for the alumina were taken from the manufacturer Ortech Advanced Ceramics [15].

Table B. 1. Temperature dependent heat capacities for Bi, Sn, and Zr [14].

Temperature	Bi (J/(kg*K))	Sn (J/(kg*K))	Zr (J/(kg*K))
296.15	121.3	230	286.1
298.15	121.5	230.2	286.2
303.15	121.7	230.9	286.8
308.15	122.0	231.5	287.3
313.15	122.2	232.1	287.9
318.15	122.5	232.8	288.4
323.15	122.7	233.5	289.0
328.15	123.0	234.2	289.6
333.15	123.2	234.8	290.3
338.15	123.5	235.5	290.8
343.15	123.7	236.2	291.4
348.15	124.0	237	292.0
353.15	124.2	237.7	292.2
358.15	124.5	238.4	293.1
363.15	124.7	239.1	293.4
368.15	125.0	239.8	294.1
373.15	125.2	240.5	294.6
378.15	125.5	241.3	295.1
383.15	125.7	242	295.8
388.15	125.9	242.7	296.3
393.15	126.2	243.5	296.9
398.15	126.4	244.2	297.4
403.15	126.7	245	298.1
408.15	126.9	245.7	298.8
413.15	127.2	246.5	299.5
418.15	127.4	247.2	300.1
423.15	127.6	248	300.3
428.15	127.9	248.8	301.0
433.15	128.1	249.6	301.2
438.15	128.4	250.5	301.7

443.15	128.6	251.3	301.9
448.15	128.8	252.2	301.8
453.15	129.1	253.1	301.7
458.15	129.3	254.0	301.8
463.15	129.6	255.0	301.9
468.15	129.8	256.0	302.0
473.15	130.0	257.0	302.6
478.15	130.3		302.7
483.15	130.5		303.1
488.15	130.7		303.8
493.15	131.0		303.8
498.15	131.2		304.6
503.15	131.4		305.0
508.15	131.7		305.5
513.15	131.9		306.1
518.15	132.1		306.6
523.15	132.3		306.9
528.15			307.5
533.15			308.1
538.15			308.5
543.15			309.1
548.15			309.6
553.15			310.1
558.15			310.5
563.15			310.8
568.15			311.4
573.15			311.9
578.15			312.4
583.15			313.1
588.15			313.8
593.15			314.1
598.15			314.5
603.15			315.2
608.15			315.8
613.15			316.4
618.15			316.7
623.15			317.5
628.15			318.1
633.15			318.5
638.15			318.9
643.15			319.3

648.15			320
653.15			320.5
658.15			320.9
663.15			321.7
668.15			322.2
673.15			322.8

Table B. 2. Temperature dependent specific heat for Si [5]

Temperature (°C)	Specific Heat (J/(kg*K))
10	692.4
20	705.2
30	718.0
40	729.9
50	741.5
60	752.0
70	760.8
80	767.9
90	774.2

Table B. 3. Specific heats for alumina and Al [15].

Material	Specific Heat (J/(kg*K))
Alumina	1300
Al	786.0

Table B. 4. Densities of Bi, Sn, Zr, Si, Alumina, and Al.

Material	Density (kg/m^3)
Bismuth	9410
Sn	7454
Zr	6844
Si	2196
Alumina	3690
Al	2700

Table B. 5. Temperature dependent thermal conductivity of Bi [16].

Temperature (K)	Thermal Conductivity (W/(m*K))
20	90.0
25	69.5
30	56.8
35	47.8
40	41.4
45	36.5
50	32.6
60	26.8
70	23.1
80	20.3
90	18.2
100	16.5
150	11.8
200	9.69
250	8.54
273	8.20
298	7.89
300	7.87
350	7.39
400	7.04
500	6.63
544.6	6.50

Table B. 6. Temperature dependent thermal conductivity of Si [21].

Temperature (K)	Thermal Conductivity (W/(m*K))
273	168
298	149
300	148
350	119
400	98.9
500	76.2
600	61.9
700	50.8
800	42.2
900	35.9
1000	31.2
1100	27.9
1200	25.7
1300	24.4

1400	23.5
1500	22.7
1600	22.1
1685	22

Table B. 7. Temperature dependent thermal conductivity of Sn [17].

Temperature (K)	Thermal Conductivity (W/(m*K))
273	68.2
298	66.8
300	66.6
350	64.2
400	62.2
500	59.6
505.1	59.5

Table B. 8. Temperature dependent thermal conductivity of Zr [18].

Temperature (K)	Thermal Conductivity (W/(m*K))
273	23.2
300	22.7
350	22.1
400	21.6
500	21

Table B. 9. Thermal Conductivities of Alumina and Al.

Material	Thermal Conductivity (W/(m*K))
Alumina	30
Al	167

Table B. 10. Thermal Emissivities.

Material	Thermal Emissivity (ϵ)
Bi	0.05
Si	1
Sn	0.04
Zr	1

Appendix C: Calorimeter Response Comparison

One set of experiments sought to examine how different the responses of two calorimeters in the same pulse could be. In these experiments two of each type of calorimeter were placed in the central cavity of the ACRR. The ACRR was pulsed three times at different yields. Figures C.1-C.12 show the results of the experiment. Although each of the calorimeters compared experienced the same pulse and were manufactured the same way, the temperatures measured by the TCs are different. This can be seen particularly in the Sn calorimeters shown in Fig. C.5-C.8, where the change in temperature measured by the two calorimeters was different by as much as 8.1%.

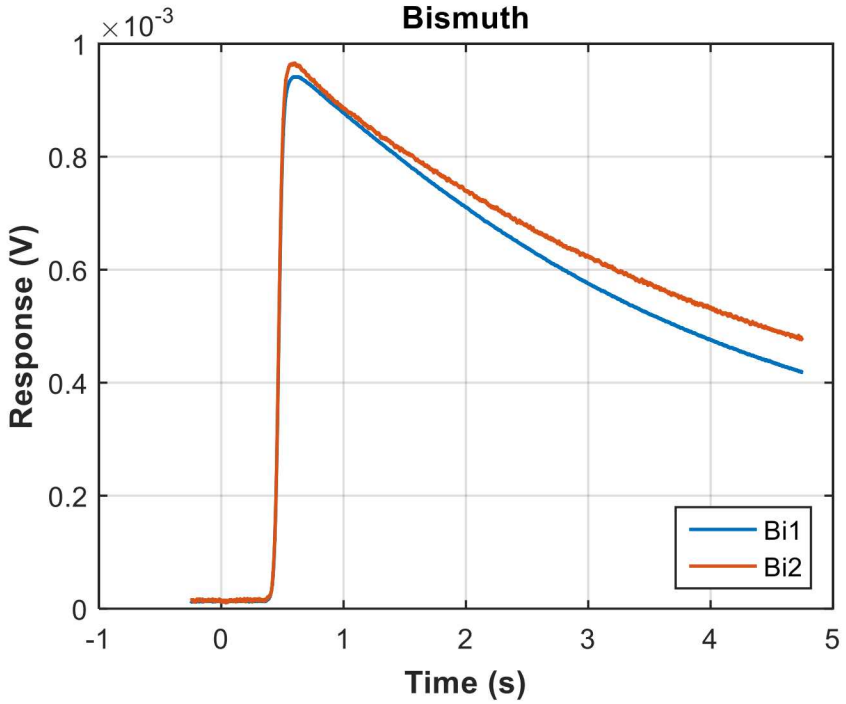

Figure C. 1. Bi calorimeter response comparison 24.4 MJ shot.

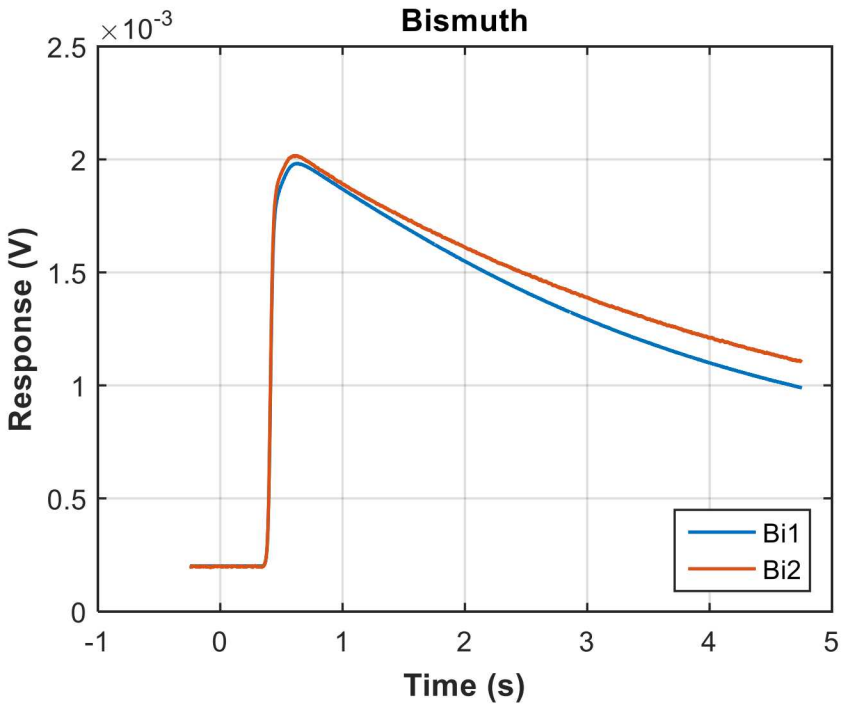

Figure C. 2. Bi calorimeter response comparison 46.9 MJ shot.

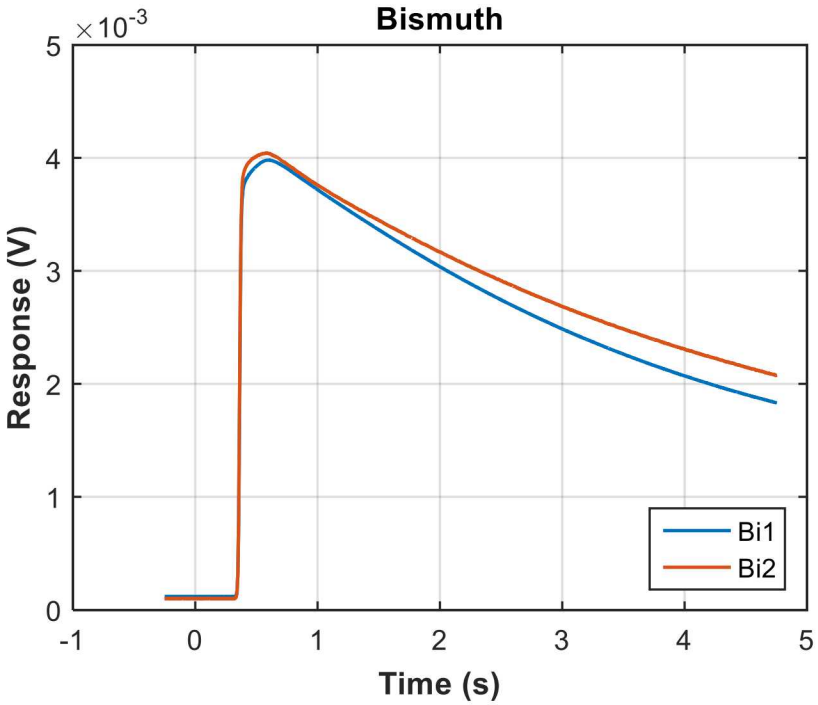

Figure C. 3. Bi calorimeter response comparison 100.9 MJ shot.

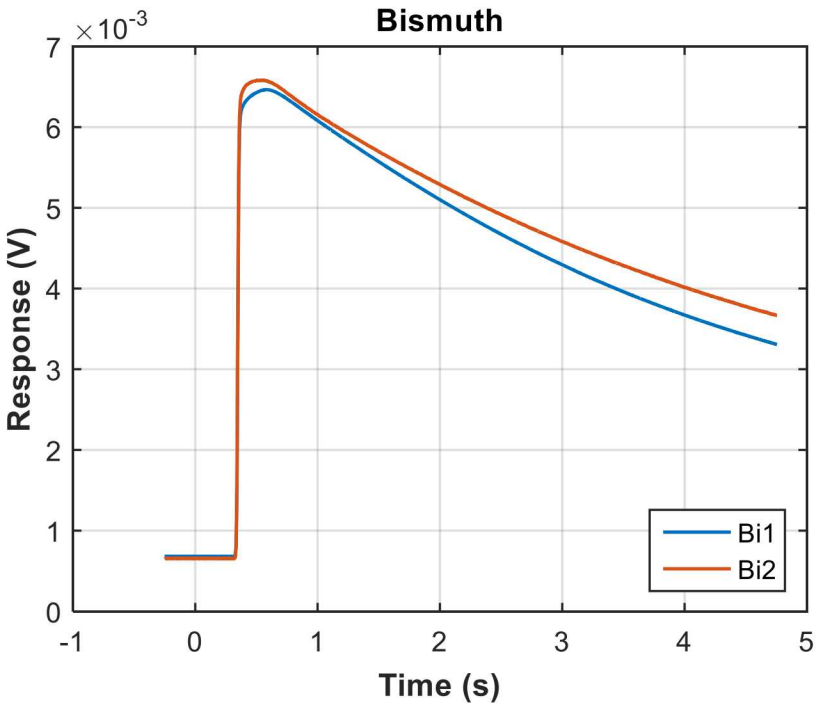

Figure C. 4. Bi calorimeter response comparison 155.4 MJ shot.

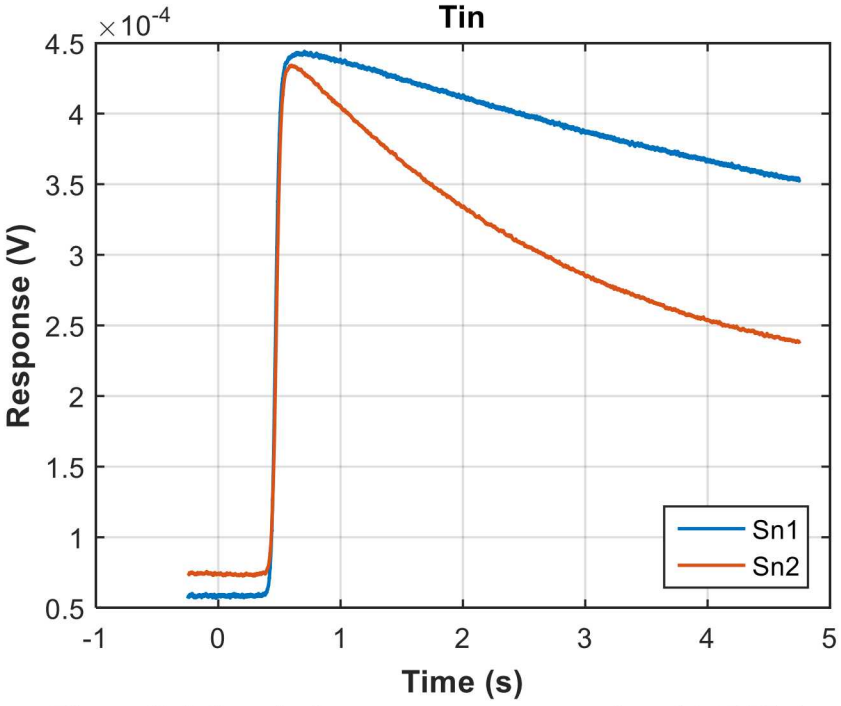

Figure C. 5. Sn calorimeter response comparison 24.4 MJ shot.

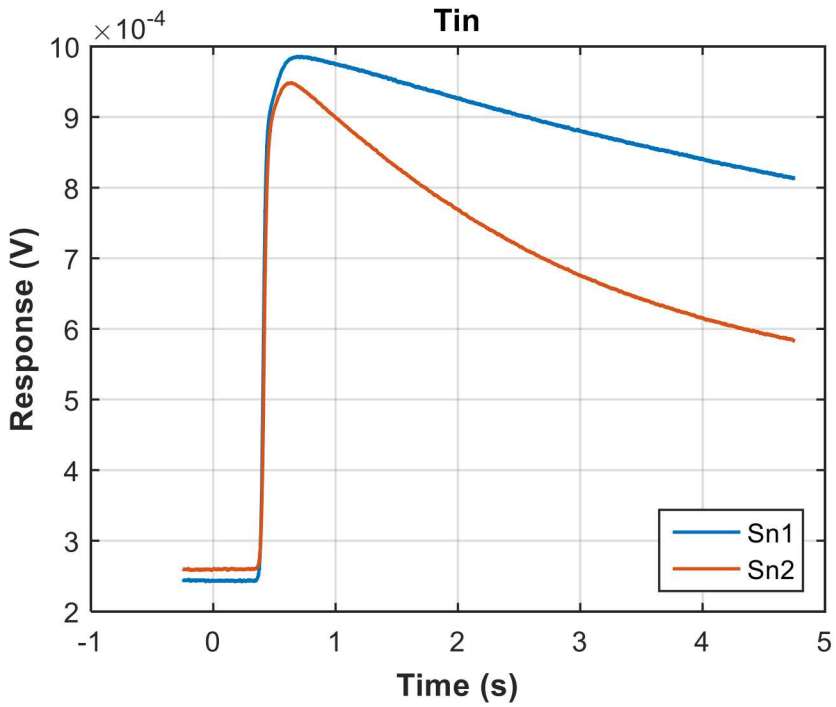

Figure C. 6. Sn calorimeter response comparison 46.9 MJ shot.

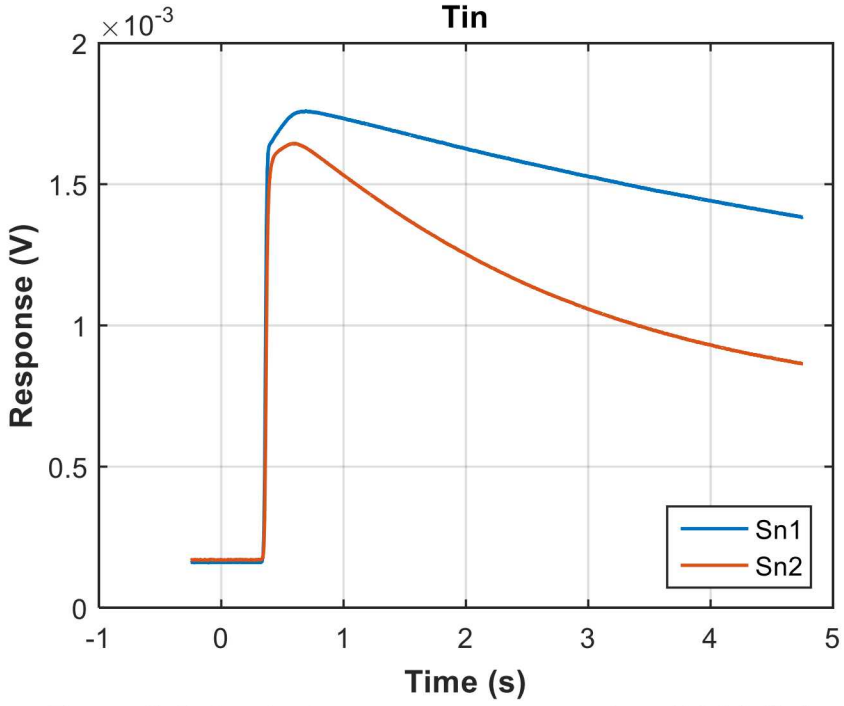

Figure C. 7. Sn calorimeter response comparison 100.9 MJ shot.

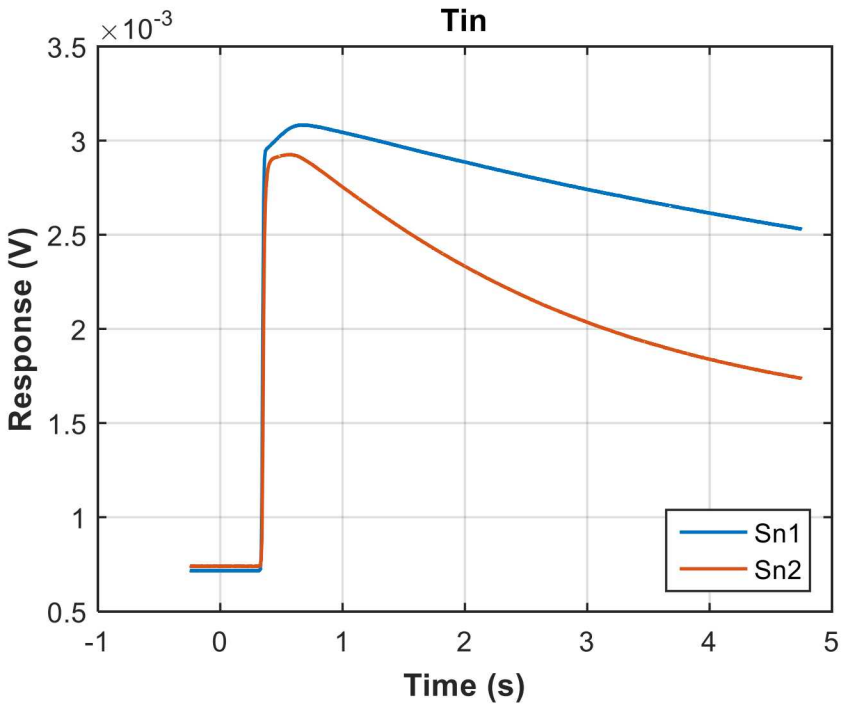

Figure C. 8. Sn calorimeter response comparison 155.4 MJ shot.

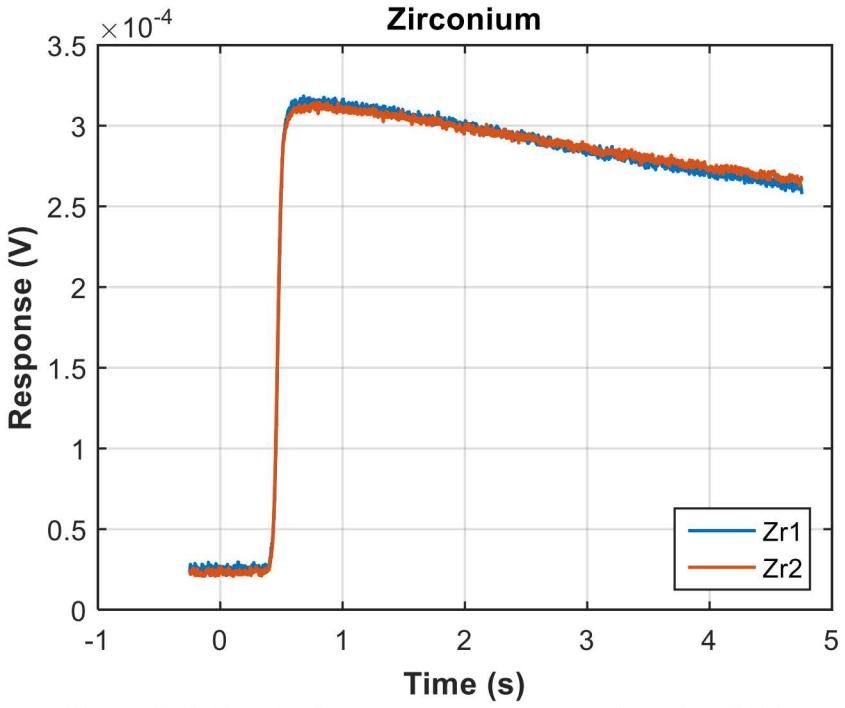

Figure C. 9. Zr calorimeter response comparison 24.4 MJ shot.

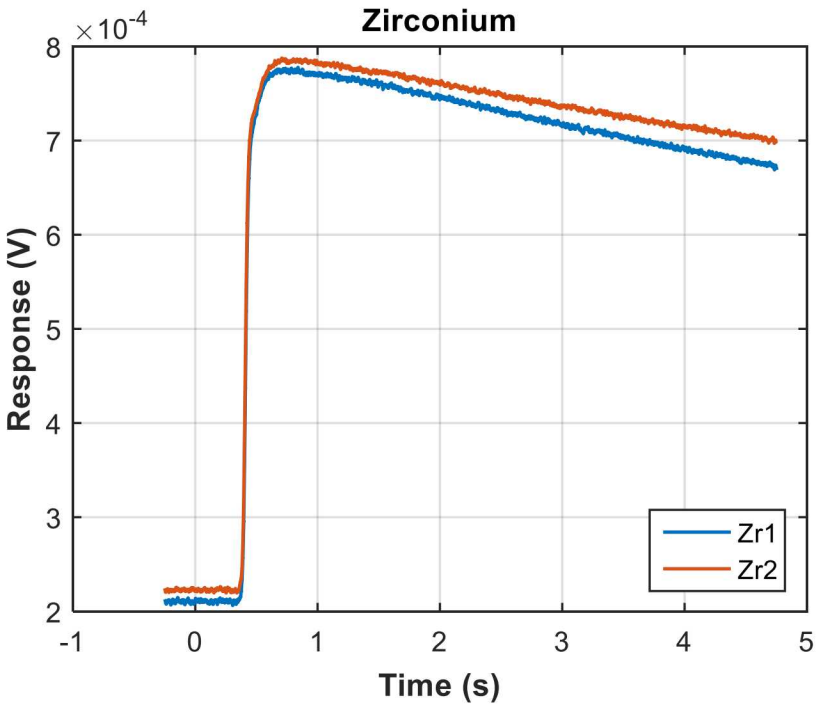

Figure C. 10. Zr calorimeter response comparison 46.9 MJ shot.

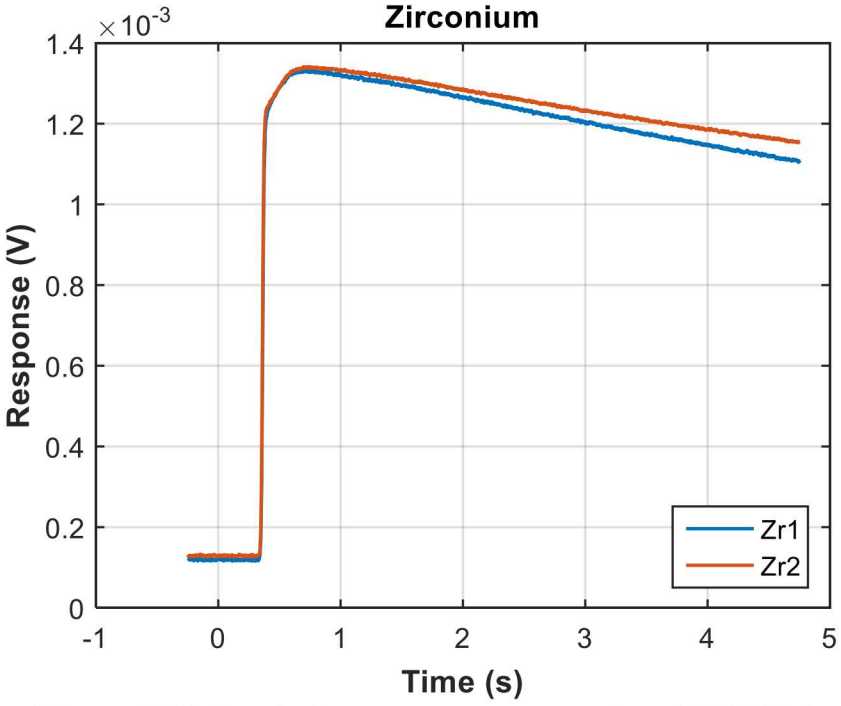

Figure C. 11. Zr calorimeter response comparison 100.9 MJ shot.

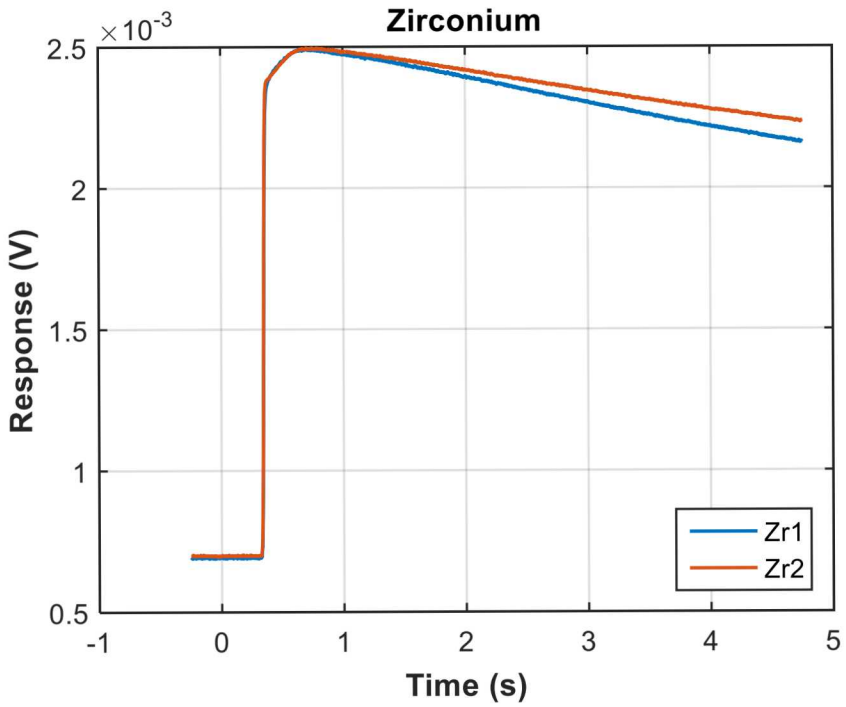

Figure C. 12. Zr calorimeter response comparison 155.4 MJ shot.

Appendix D: Specific Heat Comparison

Figures D.1- D.3 show the specific heats measured by TPRL, Inc. compared to specific heats collected from CINDAS material database for Bi, Sn, and Zr.

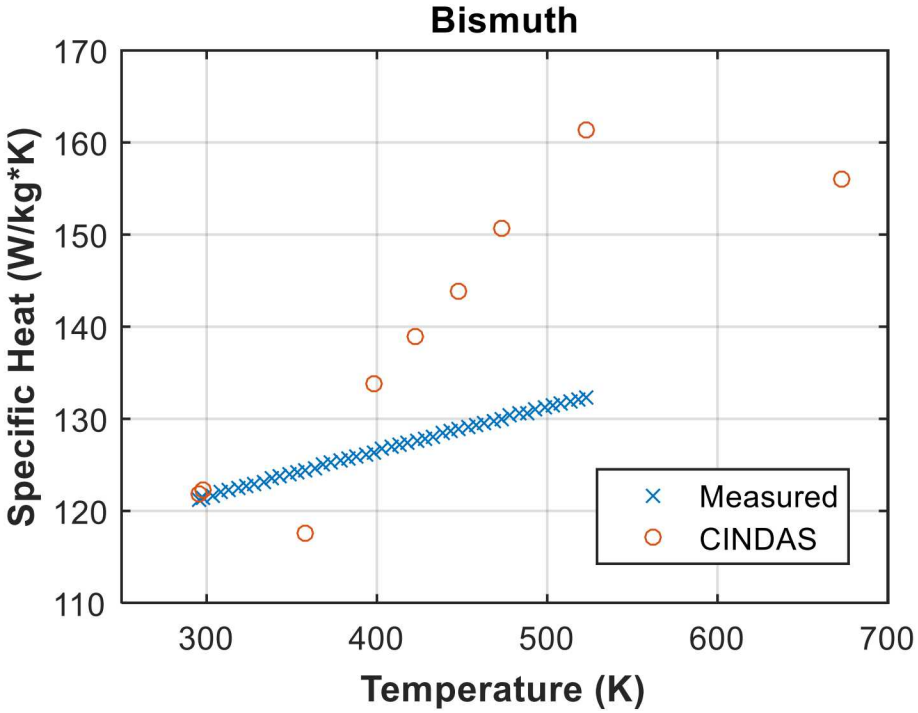

Figure D. 1. Bi specific heat comparison.

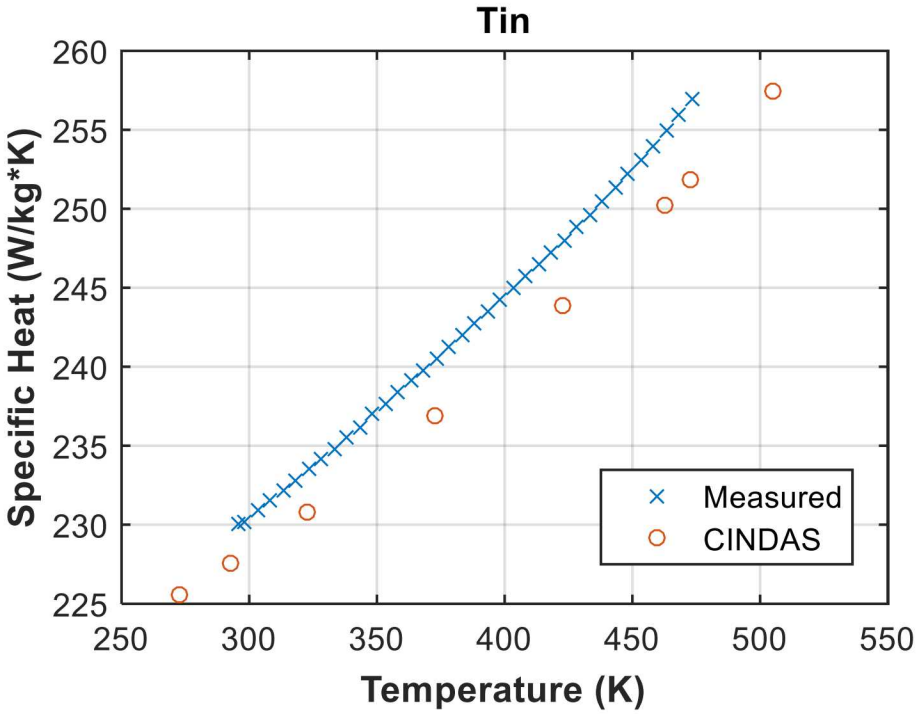

Figure D. 2. Sn specific heat comparison.

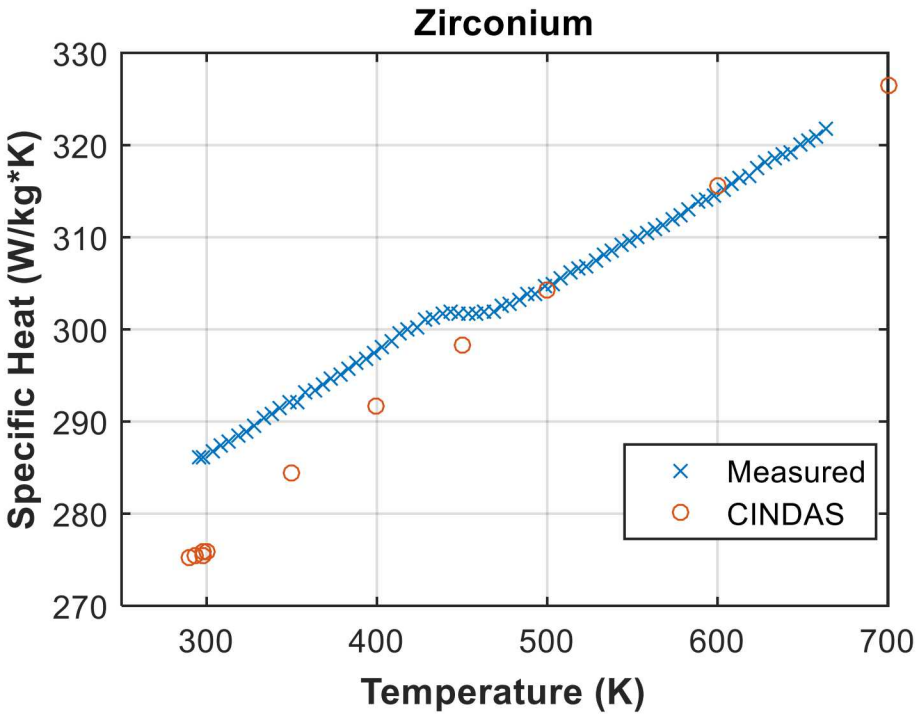

Figure D. 3. Zr specific heat comparison.

Appendix E: Radiation Contributions

The contributions of each type of radiation was found using MCNP and plotted in Figs. E.1- E.4. The most notable contribution is the delayed gamma radiation. The delayed gamma radiation can account for up to 31.23% of the total amount of energy deposited into the calorimeter. This amount of energy deposited into a perfect calorimeter would be non-negligible however the disks start to lose heat long before most the energy is deposited. This means that instead of contributing 31.23% of the measured energy it contributes less than 2% by the time heat loss dominates in the calorimeter. Figures E.5 and E.6 demonstrate that heat loss dominates after about 0.85 seconds. Figure E.5 shows a pulse with a rod hold up time of 0.4 seconds and Figure E.6 shows a pulse with a rod hold up time of 0.25 seconds. The rod hold-up time influences the shape of the pulse and thus the calorimeter response.

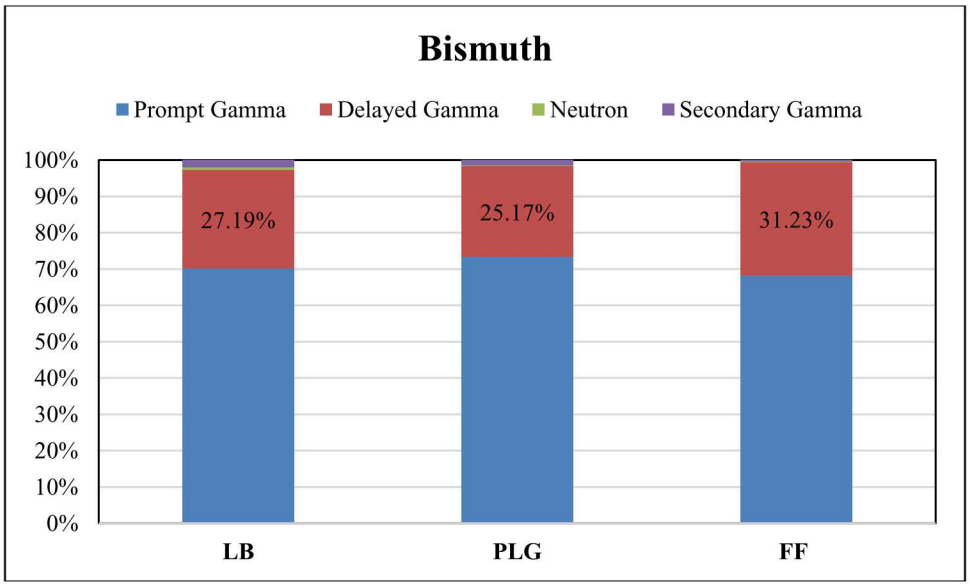

Figure E. 1. Radiation contributions for the Bi Calorimeter in FF, PLG, LB44 environments.

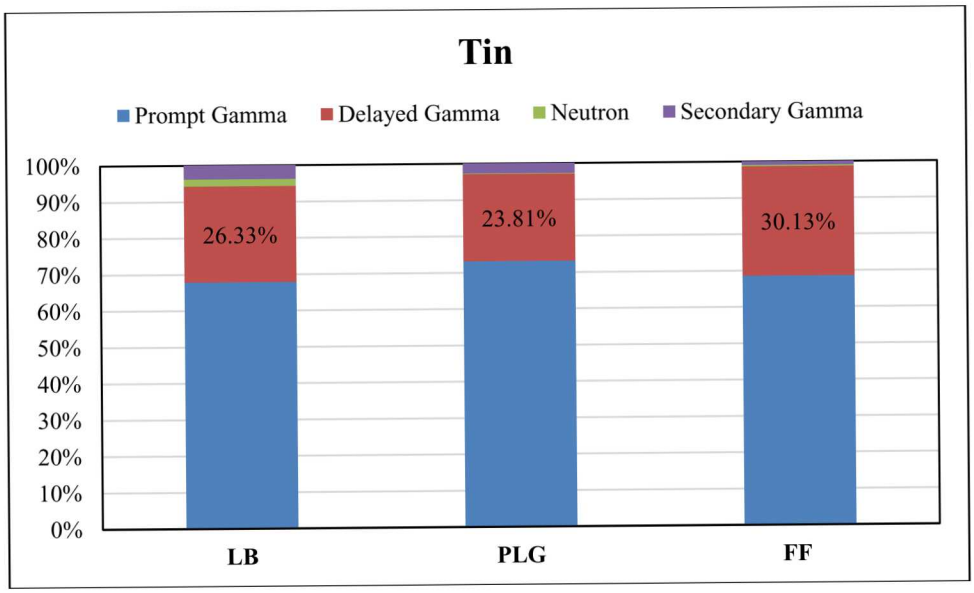

Figure E. 2. Radiation contributions for the Sn Calorimeter in FF, PLG, LB44 environments.

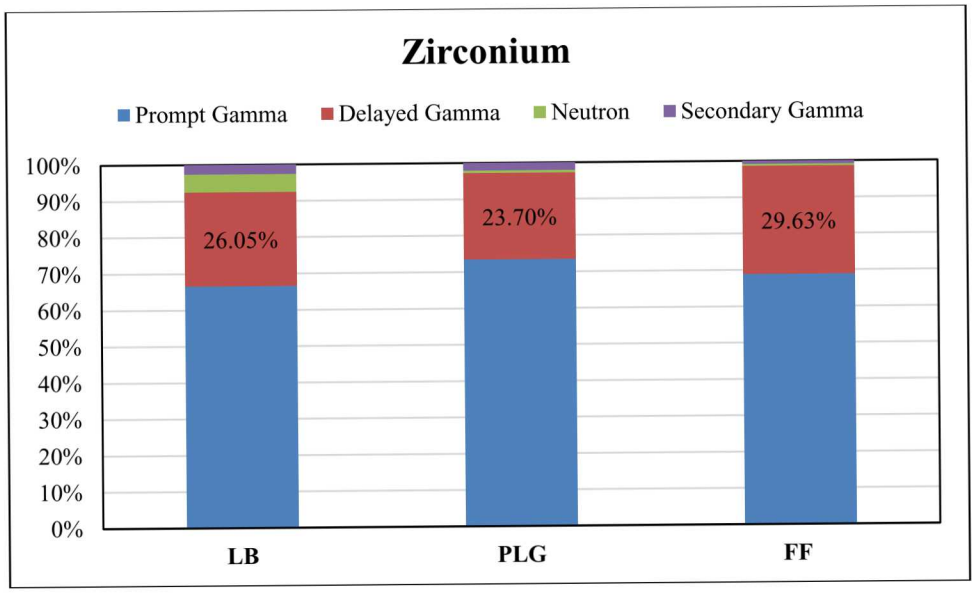

Figure E. 3. Radiation contributions for the Zr Calorimeter in FF, PLG, LB44 environments.

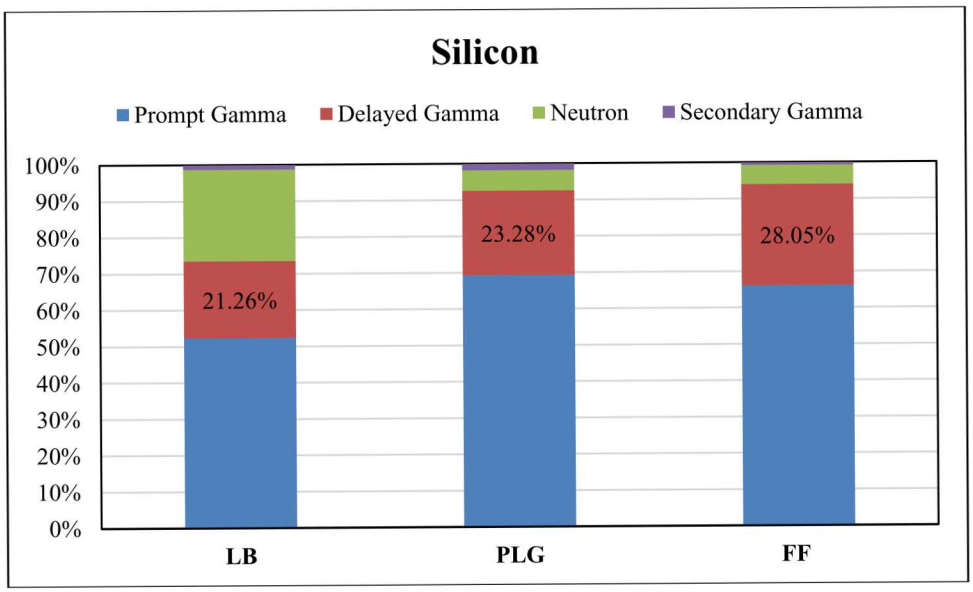

Figure E. 4. Radiation contributions for the Si Calorimeter in FF, PLG, LB44 environments.

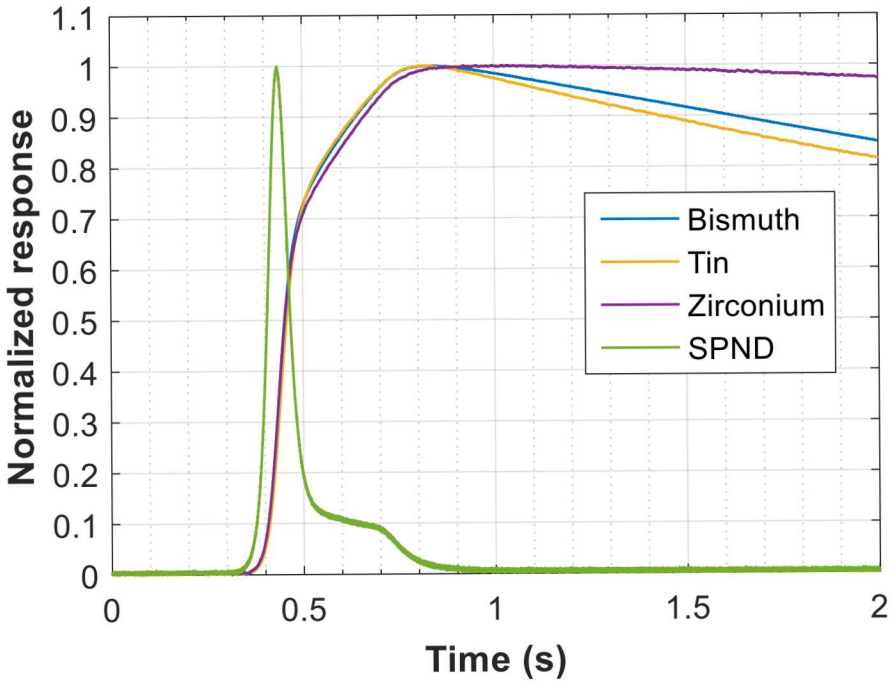

Figure E. 5. 25 MJ shot with a rod hold up time of 0.40 seconds.

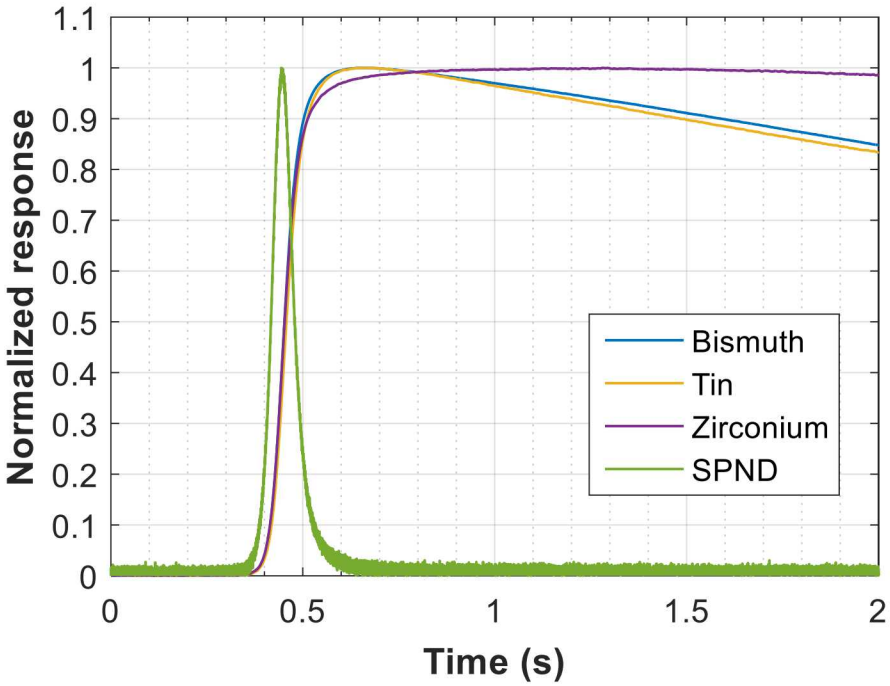

Figure E. 6. 25 MJ shot with a rod hold up time of 0.25 seconds.

References

[1] B. D. Hehr, E. J. Parma, C. D. Peters, G. E. Naranjo, and S. M. Luker, "Characterization of Novel Calorimeters in the Annular Core Research Reactor," *EPJ Web Conf.*, vol. 106, p. 01001, 2016.

[2] E. J. Parma, T. J. Quirk, L. L. Lippert, P. J. Griffin, G. E. Naranjo, and S. M. Luker, "Radiation Characterization Summary: ACRR 44-Inch Lead-Boron Bucket Located in the Central Cavity on the 32-Inch Pedestal at the Core Centerline (ACRR-LB44-CC-32-cl)," Sandia National Laboratories, Albuquerque, New Mexico, Technical Report SAND2013-3406, 2013.

[3] E. J. Parma *et al.*, "Radiation Characterization Summary: ACRR Cadmium-Polyethylene (CdPoly) Bucket Located in the Central Cavity on the 32-Inch Pedestal at the Core Centerline (ACRR-CdPoly-CC-32-cl)," Sandia National Laboratories, Albuquerque, New Mexico, Technical Report SAND2016-10114, 2016.

[4] E. J. Parma, G. E. Naranjo, R. M. Vega, L. L. Lippert, D. W. Vehar, and P. J. Griffin, "Radiation Characterization Summary: ACRR Central Cavity Free-Field Environment with the 32-Inch Pedestal at the Core Centerline (ACRR-FF-CC-32-cl)," Sandia National Laboratories, Albuquerque, New Mexico, Technical Report SAND2015-6483, 2015.

[5] E. J. Parma *et al.*, "Radiation Characterization Summary: ACRR-FRECII Cavity Free-Field Environment at the Core Centerline (ACRR-FRECII-FF-cl)," Sandia National Laboratories, Albuquerque, New Mexico, Technical Report SAND2017-8674, 2017.

[6] E. J. Parma, D. W. Vehar, L. L. Lippert, P. J. Griffin, G. E. Naranjo, and S. M. Luker, "Radiation Characterization Summary: ACRR Polyethylene-Lead-Graphite (PLG) Bucket Located in the Central Cavity on the 32-Inch Pedestal at the Core Centerline (ACRR-PLG-CC-32-cl)," Sandia National Laboratories, Albuquerque, New Mexico, Technical Report SAND2015-4844, 2015.

[7] S. M. Luker *et al.*, "Development of a Silicon Calorimeter for Dosimetry Applications in a Water-Moderated Reactor," *J. ASTM Int.*, vol. 3, no. 10, pp. 1–9, Nov. 2006.

[8] "SOLIDWORKS Simulation Help," Dassault Systèmes SolidWorks Corporation, Waltham, Mass., User's Guide, 2014.

[9] "Ansys 18.2 Workbench User's Guide," ANSYS, Inc, Canonsburg, Pa, User's Guide.

[10] D. B. Pelowitz, Ed., *MCNP6 USER'S MANUAL*. Los Alamos, New Mexico: Los Alamos National Security, LLC, 2008.

[11] T. K. Lane and E. J. Parma, "Delayed Fission Gamma-ray Characteristics of 232Th, 233U, 235U, 238U, and 239Pu.," Sandia National Laboratories, Albuquerque, New Mexico, Technical Report SAND2015-7024, 2015.

[12] W. H. Todt, "Characteristics of Self-Powered Neutron Detectors Used in Power Reactors," Imaging and Sensing Technology Corporation, Horseheads, New York, Technical Report.

[13] A. Savitzky and M. J. E. Golay, "Smoothing and Differentiation of Data by Simplified Least Squares Procedures.," *Anal. Chem.*, vol. 36, no. 8, pp. 1627–1639, Jul. 1964.

[14] R. Larsen, "Specific Heat of Three Samples: A report to Sandia National Laboratory," TPRL, Inc., West Lafayette, IN, TPRL 5512, Mar. 2017.

[15] "Alumina Oxide Ceramics Al2O3 – properties & applications," *Advanced Ceramic Manufacturer*. .

[16] "Bismuth: CINDAS Recommended Data Based on CINDAS Evaluation from Available Information," *CINDAS LLC Thermophysical Properties of Matter Database*. [Online].

Available: https://cindasdata.com/Applications/TPMD/?action=+Show+Text+&subaction=&mgcode=&pgcode=&mcode=00006&mname=bismuth&pname=&pcode=0101&indvar=0601&prop_and_indvar=0101%3A0601&prop_range_min=&prop_range_max=&gridlines=0&smcode%3Alist=00006&datasets%3Alist=2356.

[17] "Tin: CINDAS Recommended Data Based on CINDAS Evaluation from Avaiable Information." [Online]. Available: https://cindasdata.com/Applications/TPMD/?action=+Show+Text+&subaction=&mgcode=&pgcode=&mcode=00071&mname=tin&pname=&pcode=0101&indvar=0601&prop_and_indvar=0101%3A0601&prop_range_min=&prop_range_max=&gridlines=0&smcode%3Alist=00071&datasets%3Alist=2413.

[18] "Zirconium: CINDAS Recommended Data Based on CINDAS Evaluation from Avaiable Information." [Online]. Available: https://cindasdata.com/Applications/TPMD/?action=+Show+Text+&subaction=&mgcode=&pgcode=&mcode=00079&mname=zirconium&pname=&pcode=0101&indvar=0601&prop_and_indvar=0101%3A0601&prop_range_min=&prop_range_max=&gridlines=0&smcode%3Alist=00079&datasets%3Alist=2421.

[19] "Table of Total Emissivity." Omega.

[20] "Convection Heat Transfer Coefficients Equations and Calculator | Engineers Edge | www.engineersedge.com." [Online]. Available: http://www.engineersedge.com/heat_transfer/convection_heat_transfer_coefficients_13855.htm. [Accessed: 02-Oct-2017].

[21] H. M. Roseberk, "The Thermal Conductivity Of Germanium And Silicon At Low Temperatures," *CINDAS LLC Thermophysical Properties of Matter Database*, 1954. [Online]. Available: https://cindasdata.com/Applications/TPMD/?action=+Show+Graph+&subaction=&mgcode=&pgcode=&mcode=00059&mname=silicon&pname=&pcode=0101&indvar=0601&prop_and_indvar=0101%3A0601&prop_range_min=&prop_range_max=&newaction=+Show+Text+&smcode%3Alist=00059&sdatacurves%3Alist=2403%3A1.

Distribution

1	MS1146	Brandon Aguirre	1384(electronic copy)
1	MS1146	Thomas Ball	1384(electronic copy)
1	MS1136	Rodney Keith	8841(electronic copy)
1	MS1136	Billy Martin	1384(electronic copy)
1	MS1146	Edward Parma	1384
2	MS1146	Elliott Pelfrey	1384
1	MS1136	Curtis Peters	8841(electronic copy)
1	MS1146	Jesse Roebuck	1384(electronic copy)
1	MS0899	Technical Library	9536 (electronic copy)


Sandia National Laboratories